The break of earthquake asperities imaged by distributed acoustic sensing

https://doi.org/10.1038/s41586-023-06227-w

Jiaxuan Li^{1⊠}, Taeho Kim², Nadia Lapusta^{1,2}, Ettore Biondi¹ & Zhongwen Zhan¹

Received: 18 October 2022

Accepted: 16 May 2023

Published online: 2 August 2023



Check for updates

Rupture imaging of megathrust earthquakes with global seismic arrays revealed frequency-dependent rupture signatures ¹⁻⁴, but the role of high-frequency radiators remains unclear³⁻⁵. Similar observations of the more abundant crustal earthquakes could provide critical constraints but are rare without ultradense local arrays^{6,7}. Here we use distributed acoustic sensing technology^{8,9} to image the high-frequency earthquake rupture radiators. By converting a 100-kilometre dark-fibre cable into a 10,000-channel seismic array, we image four high-frequency subevents for the 2021 Antelope Valley, California, moment-magnitude 6.0 earthquake. After comparing our results with long-period moment-release 10,11 and dynamic rupture simulations, we suggest that the imaged subevents are due to the breaking of fault asperities-stronger spots or pins on the fault—that substantially modulate the overall rupture behaviour. An otherwise fading rupture propagation could be promoted by the breaking of fault asperities in a cascading sequence. This study highlights how we can use the extensive pre-existing fibre networks¹² as high-frequency seismic antennas to systematically investigate the rupture process of regional moderate-sized earthquakes. Coupled with dynamic rupture modelling, it could improve our understanding of earthquake rupture dynamics.

A better understanding of earthquake rupture and fault physics relies on improving earthquake imaging, a challenging remote-sensing problem. Back-projection of far-field (teleseismic) waves using dense seismic arrays across continents has enabled a detailed examination of the complex rupture propagation of great earthquakes^{1,2,13,14}. For example, the imaged high-frequency radiators are often offset from the high-slip areas for large megathrust earthquakes²⁻⁵. The high-frequency energy bursts are argued to originate from the breakage of smaller asperities on the fault plane¹⁵⁻¹⁷. For the more frequent smaller earthquakes, high-frequency information is lost in far-field recordings, and near-field imaging is challenging owing to complex seismic waveforms. Specially designed ultradense seismic arrays around active faults have enabled back-projection imaging to resolve smaller features in moderate-sized earthquakes^{6,7}. Aback-projection study of the 2004 Parkfield, California, moment magnitude (M_w) 6.0 earthquake imaged a high-frequency radiator from the high-slip-gradient area and suggested that it represents the breaking of an asperity that initiates large moment release seen in long-period inversions⁶. However, such observations are rare as ultradense seismic arrays near earthquakes are usually not available. Hence it is unknown how frequent such high-frequency subevents are in crustal earthquakes and whether and how they affect the overall rupture. The underlying fault heterogeneity may control foreshocks, rupture initiation and $propagation^{15-22}, and \, whether \, earthquake \, size \, can \, be \, determined \, from \,$ the early rupture phases is a question of substantial interest²³⁻²⁶.

In this study, we use recordings from an ultradense distributed acoustic sensing (DAS) array converted from pre-existing telecommunication fibre-optic cables to image the earthquake rupture process^{8,9}. We identify the high-frequency radiators of an $M_{\rm w}$ 6.0 crustal earthquake that occurred on 8 July 2021, at a depth of 7.5 km in the Antelope Valley, Northern California, close to the California-Nevada border. It was the fourth earthquake above $M_{\rm w}$ 6 in the Walker Lane, an approximately 100-mile-wide fault zone between the Sierra geomorphic province and the Basin and Range²⁷⁻²⁹, in the past two decades. The other three earthquakes are the 2019 Ridgecrest M_w 6.4 and M_w 7.1 earthguakes (depth of 10.5 km and 8.0 km, respectively), and the $2020 M_{\rm w}$ 6.5 Monte Cristo Range earthquake (depth of 2.7 km). The focal mechanism and early aftershocks of the Antelope Valley $M_{\rm w}$ 6.0 event indicate a north-striking normal faulting plane dipping to the east (Fig. 1). Its moment-rate function, determined using long-period waveforms, has a duration of about 10 s and multiple peaks 10,11,30, which is relatively long and complex compared with earthquakes of similar magnitude and depth range^{10,31} (Extended Data Fig. 1).

Back-projection rupture imaging with DAS

The earthquake was recorded by the 100-km-long Long Valley DAS array, which consists of two 50-km sections of telecom dark fibre to the north and south of the town of Old Mammoth (Fig. 1). The 10,000 channels of the array are continuously sampled at 200 Hz and distributed in 10-m spacing between Mono Lake and Crowley Lake, mostly along the US-395 Highway. The DAS recording of the $M_{\rm w}$ 6.0 mainshock shows mostly unsaturated P and S wavefields (Fig. 2a).

This rare dataset allows us to apply back-projection to identify high-frequency radiators in a moderate-sized earthquake with a DAS

Seismological Laboratory, Division of Geological and Planetary Sciences, California Institute of Technology, Pasadena, CA, USA. Mechanical and Civil Engineering, Division of Engineering and Applied Science, California Institute of Technology, Pasadena, CA, USA. [™]e-mail: jxli@caltech.edu

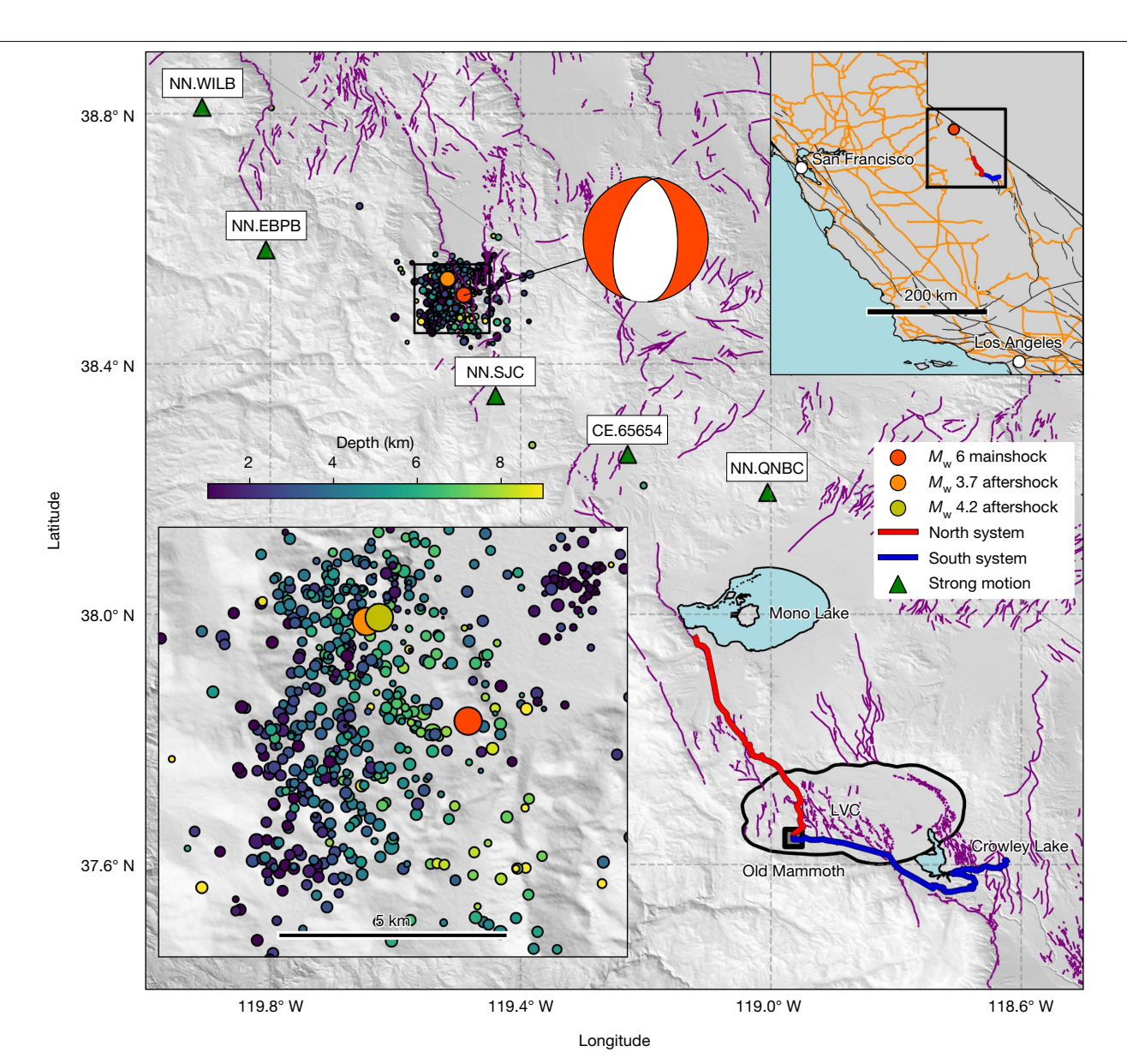


Fig. 1 | A 100-km fibre-optic cable as a dense DAS local array for imaging of a regional moderate crustal earthquake. The 2021 Antelope Valley $M_{\rm w}$ 6.0 earthquake (red circle; focal mechanism shown by the red-and-white ball) occurred to the northwest of the DAS systems, within the central part of the Walker Lane fault zone hosting many faults (solid purple lines). The north DAS system (red line) starts from the Old Mammoth and extends towards the northwest. The south DAS system (blue line) extends to the east on the fringe of the Long Valley Caldera (LVC, indicated by the black closed curve). Many aftershocks occurred around the mainshock faulting plane dipping to the east

(the black square enlarged in the bottom-left corner); the $M_{\rm w}$ 3.7 and $M_{\rm w}$ 4.2 aftershock events (orange and dark yellow circles) are used as EGFs. Five strong-motion stations (green triangles, with their respective network and station names indicated in white boxes above) recorded unclipped data of the mainshock within a 70-km epicentral distance. The 100-km fibre-optic cable used in this study represents a small portion of the current and proposed telecommunication fibre network (for example, the 10,000-mile State of California Middle-Mile Broadband Initiative indicated by orange lines in the top right inset map)39.

array (Fig. 2b). The details of the method that we have developed specifically for DAS data can be found in Methods; here we briefly mention the key ingredients. In contrast with the teleseismic P-wave back-projection imaging that is performed on a two-dimensional horizontal plane, with the depth interpretation relying purely on the mapping of the two-dimensional image onto a pre-known fault geometry³², we use both P and S waves simultaneously to constrain subevent locations in the three-dimensional (3D) space, because both still retain high-frequency energy in the range of 1-5 Hz. To mitigate inaccuracies in local velocity models and accommodate the more complex waveforms owing to shallow crustal heterogeneities, we use DAS waveforms of aftershocks as empirical Green's functions (EGFs) to replace the Dirac delta function or synthetic Green's functions used in conventional or hybrid

back-projection^{1,33}. More specifically, we first cross-correlate the mainshock and selected aftershock waveforms at each DAS channel and then back-project the correlation functions (Extended Data Fig. 2a,b). Therefore, the subevent locations we derive are relative to the selected aftershocks and less dependent on the picking and alignment of the event P and S onset in data.

Our imaging reveals four high-frequency subevents during the $M_{\rm w}$ 6.0 earthquake (Methods and Extended Data Fig. 3i). The relatively weak first subevent SO (Extended Data Fig. 4a,e) has a similar origin time and location as the hypocentre of the $M_{\rm w}$ 6.0 mainshock in the United States Geological Survey (USGS) catalogue. Subevent S1 occurs about 0.6 s after subevent SO and appears as a distinct peak in the correlation function profiles (Extended Data Fig. 2a). The peak stacks most

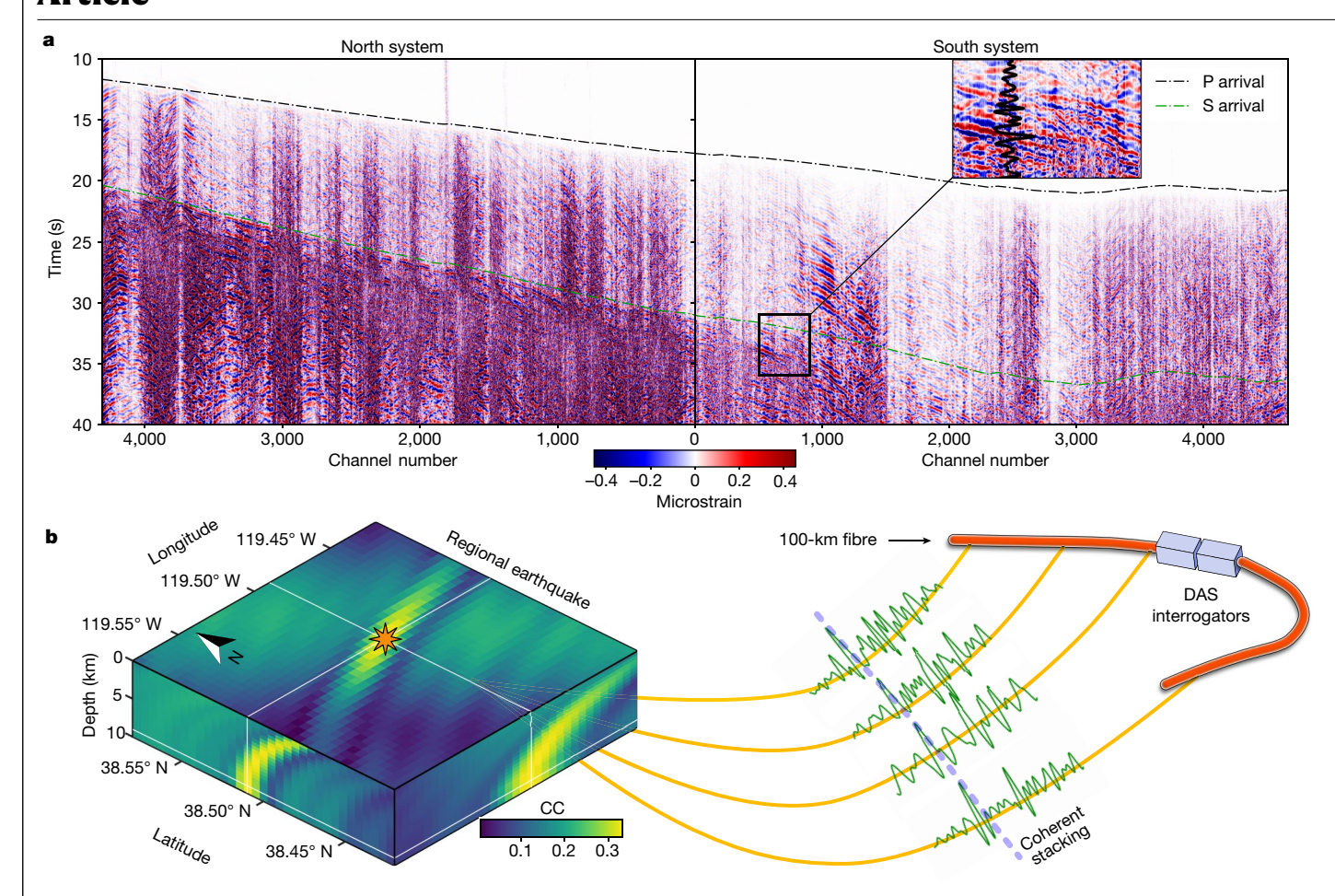


Fig. 2 | Seismic recordings on thousands of closely spaced channels of the DAS array that reveal the presence of subevents in the $M_{\rm w}$ 6.0 earthquake. a, Seismic records (microstrain) from the north and south DAS systems of the $M_{\rm w}$ 6.0 event. Channel number 0 is the location of the two DAS interrogators hosted in Old Mammoth. The predicted P and S arrival times (black and green lines) using a local one-dimensional velocity model 40 match the onset of the seismic energy consistently across all channels. The inset shows the zoomed-in view of the seismic recording with the seismogram on one channel

shown in black. **b**, Schematics of the 3D imaging around the source region by back-projecting both P and S correlograms (Methods) from the channels in the 100-km-long fibre. Examples of S-phase correlograms averaged over 1,000 channels are shown in green along the yellow ray paths. The back-projected correlograms stack coherently at the subevent location, resulting in a bright spot with high cross-correlation values (CC) in the 3D volume (yellow colour in the left block).

coherently once back-projected to the preferred subevent S1 source location (Extended Data Fig. 4b, f). Similarly, for the subevents S2 and S3, back-projection of the large number of channels over a long aperture helps identify and locate them well (Extended Data Fig. 4), although the correlation peaks are not as strong (Extended Data Fig. 4c,d) owing to coda waves from the earlier subevents. Because the mainshock focal mechanism and aftershock distribution illuminate a well defined fault plane, we further constrain the subevents to be on the fault plane, by slicing the 3D back-projection volume (Extended Data Fig. 3 and Supplementary Video 1). The resulting subevent locations are in a 3-km-by-5-km area (Fig. 3b), within the slip distribution of the USGS finite-fault model of the event¹¹. The location uncertainties are low in the direction towards the DAS array because of the simultaneous use of P and S waves, and higher in the tangential direction owing to the limited azimuthal aperture (about 12°) of the fibre cable (Fig. 2b). Another DAS array at a different azimuth would substantially improve the resolution.

Validation of the imaged subevents

The location and timing of the four imaged subevents can be validated independently by the conventional seismograms nearby—specifically,

the timing of S-wave arrivals at five local strong-motion stations within an epicentral distance of 70 km (Fig. 1). The tangential components of the velocity seismograms, which highlight the high-frequency energy more than the displacement seismograms, show several strong pulses of S waves (Fig. 3c). At each station, after we shift the arrival times of the four subevents by a common amount to account for the uncertainty in the one-dimensional velocity model (Extended Data Fig. 5), we find remarkable agreements between the predicted arrival time of subevents S1-S3 and the timing of the tangential peak amplitudes in velocity seismograms at various epicentral distances and azimuths (Figs. 1 and 3c). For example, at stations SJC, 65654 and QNBC, the large peak amplitudes coincide with the predicted S-wave arrival time window of subevents S1-S3. For station EBPB, the small amplitude in the time window for subevents S1 and S2 could be caused by nodal planes of the radiation pattern. Using a simple scaling method (Extended Data Fig. 6 and Methods), we use the strong-motion recordings to estimate the magnitudes of subevents S0-S3 to be about M_w 4.3, M_w 4.6, M_w 5.2 and $M_{\rm w}$ 5.4, respectively. Their total seismic moment contributes about 20% of the total moment of this earthquake (Extended Data Fig. 3i).

Although the conventional seismic stations are quite helpful in confirming the timing and location of subevents, it is noted that one could not achieve this detailed back-projection image of the M_w 6.0

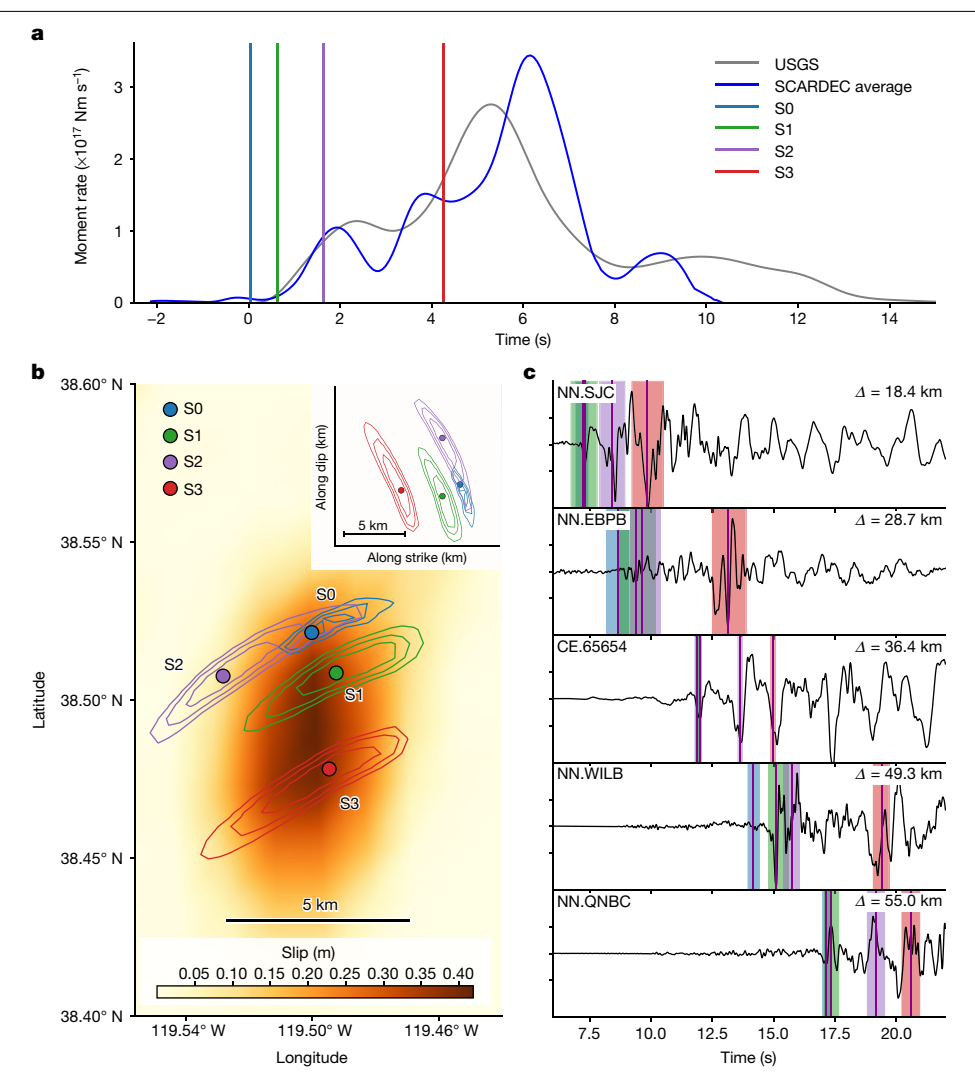


Fig. 3 | The imaged subevents in relation to the low-frequency finite-fault inversions and recordings from regional seismic stations. a, The timing of the imaged subevents (coloured vertical bars) with respect to the moment release in the earthquake as captured by the USGS (grey curve) and SCARDEC method ('seismic source characteristics retrieved from deconvolvolving teleseismic body waves') (blue curve)^{10,11} indicates that subevents occur within the first half of the event, with the last subevent potentially delaying the moment release and then being followed by the largest peak in the moment release. **b**, Map view for the back-projection locations of the subevents compared with the USGS finite-fault slip inversion (background colour), showing the subevent

locations with the highest correlations (filled circles) and the contours of 70%, 80% and 90% of the peak correlation (coloured contours). Inset: the faultplane view of the subevent locations. c, The predicted arrival time of the S phase from the subevents at five local strong-motion stations is shown on the tangential components of the velocity seismograms, from the locations with peak correlation (vertical lines) and locations with at least 70% of the peak correlations (coloured boxes). After making individual time shifts at each strong-motion station (SJC, 0.11 s; EBPB, -0.67 s; 65654, -0.12 s; WILB, -0.8 s; QNBC, -0.18 s), the arrival times coincide with seismogram peaks. The epicentral distances (Δ) of the strong-motion stations are shown in the top right corner.

event using only the conventional stations (Extended Data Fig. 7). Using seven broadband stations close to the DAS system, subevent S1 is barely detected, with much lower resolution, and the remaining three subevents are overwhelmed by the noise (Extended Data Fig. 7b). The DAS system outperforms the conventional local network owing to the large and high-density number of channels available to perform the coherent stacking for imaging high-frequency sources. We find that the detection significance increases with the number of channels used (Extended Data Fig. 7e), but the marginal gain on detection significance becomes smaller after we have more than 1,000 channels.

Physical origin of the imaged subevents

Several characteristics of the subevents offer clues to their physical origin. The subevents represent splashes of high-energy radiation as imaged by DAS, indicating abrupt local changes in the rupture

process^{19,20,34}. Such high-frequency radiation can be caused by several kinds of fault heterogeneity that would result in abrupt changes in the rupture process, including fault-friction properties and fault geometry; synthetic studies indicate that the origin of the high-frequency radiation is difficult to elucidate using back-projection results only³⁵. To gain further insight, we compare the inferences from the high-frequency DAS back-projection with the low-frequency features of the moment-release rate. First, the subevents occur when the overall moment-release rate-which corresponds to the integrated slip increment over the fault-is increasing, indicating that they promote rupture overall. Second, the largest subevent S3 occurs after a marked decrease in the moment-release rate. Third, subevent S3 is also preceded by an inferred reduction in the earthquake rupture speed (Extended Data Fig. 3i): the rupture slows down to about 30% of the shear-wave velocity before subevent S3, despite propagating with the apparent speed of about 70-80% of the shear-wave velocity between subevents S0

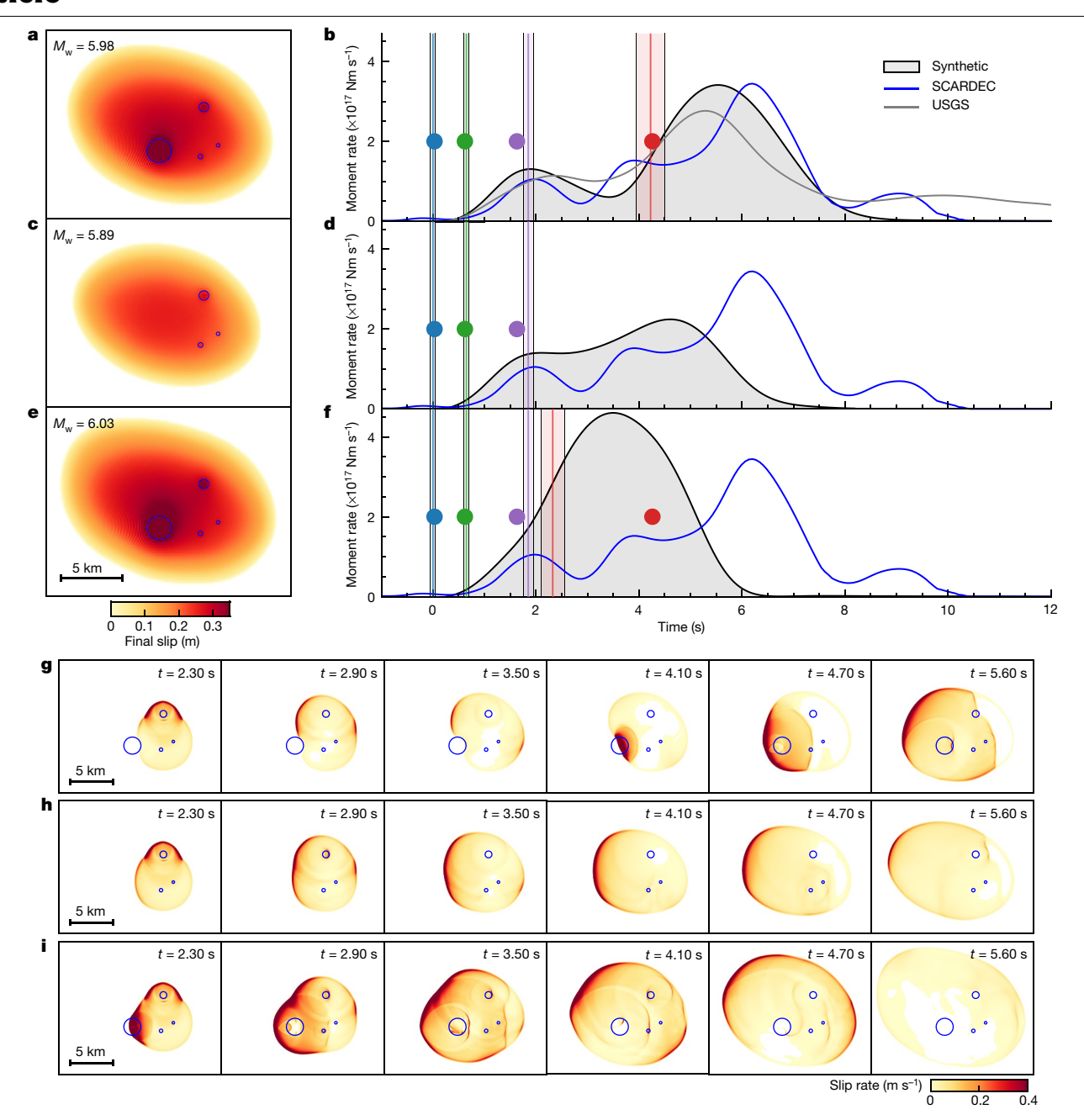


Fig. 4 | Subevents as breakage of stronger local fault patches (asperities) and their effect on rupture illustrated by dynamic rupture modelling.

a-f, Final slip (colour, **a,c,e**) and moment-rate evolution (black lines with grey shading, **b,d,f**) for three models: model 1 with four asperities that mimics the rupture process of the M_w 6 Antelope Valley event (**a,b**); model 2 with the fourth asperity removed to illustrate its effect (**c,d**); and model 3 with a weaker fourth asperity (**e,f**); the location of asperities are shown by blue circles (**a,c,e**). The simulated moment rate for the preferred model 1 (**b**) matches the main features of the ones inferred from the SCARDEC (blue curve)¹⁰ and USGS finite-fault

solutions (grey curve)¹¹. The simulated times of the rupture breaking each asperity (coloured vertical lines, with coloured boxes indicating the time range that the rupture front passes the asperity) match the occurrence time of subevents from back-projection imaging (filled circles). \mathbf{g} - \mathbf{i} , Snapshots of slip rate on the fault illuminating the rupture process for model 1 with four asperities (\mathbf{g}), model 2 with the fourth asperity removed (\mathbf{h}) and model 3 with a weaker fourth asperity (\mathbf{i}). Eliminating or changing the fourth asperity substantially affects the rupture process and overall moment release.

and S1 as well as between subevents S0 and S2. The second and third observations suggest that something impedes and delays the rupture before subevent S3 occurs. Fourth, subevent S3 is followed by the second—much larger—peak of the moment release in the earthquake.

These observations suggest that the subevents occur as breakage of stronger patches of the fault that may first act as a temporary asperity or barrier to rupture—depending on how much they are loaded interseismically—but then abruptly fail, loaded by nearby dynamic slip, and provide a boost of released energy that promotes

rupture propagation ^{19,20}. In particular, the fourth and largest asperity (subevent S3) appears to delay the rupture propagation initially, resulting in lower apparent rupture speed, but then its failure allows the fault to experience larger rupture speeds and larger slip, leading to the second larger peak in the moment release.

The presence of such stronger local patches could result from local fault non-planarity, with the compressed fault 'bumps' leading to locations of higher fault-normal stress and hence higher friction resistance. Fault patches of higher normal stress have been linked to supershear

rupture transition¹⁹, high-frequency radiation in subduction-zone earthquakes²⁰, and foreshock-like seismicity in laboratory experiments²¹ and modelling²². They can be the dominating features of the overall normal stress heterogeneity owing to fault roughness^{36,37}. Alternatively, stronger patches could be the locations of different fault rocks. with higher friction, or places of lower pore fluid pressure. Stronger fault patches lead to the complex rupture evolution discussed, not only owing to their different strength that needs to be overcome during dynamic rupture but also owing to their potential to develop different prestress; in particular, the higher strength would allow the interseismic fault loading to lead to higher local prestress, resulting in locally higher stress drops and slips during dynamic rupture. In our simulations of model 1, the average stress drop is 1.4 MPa and the stress drop over asperities ranges from 5 MPa to 6 MPa (Extended Data Fig. 9).

Inferred rupture dynamics

To illustrate how a fault with locally stronger patches can lead to rupture dynamics with subevents as captured by our observations and match low-frequency properties of the overall event, we perform dynamic rupture simulations on a rate-and-state fault³⁸. We consider a homogeneous planar seismogenic fault region that contains circular patches of higher normal stress, placed at the locations suggested by the back-projection DAS imaging (see Methods and Extended Data Table 1 for modelling parameters and procedures). The asperities increase in their size to produce increasingly larger subevents as inferred by the scaling analysis of the subevent magnitudes (Extended Data Fig. 6). We refer to this model as model 1. It reproduces several key observations: breaks of asperities radiate high-frequency slip perturbations with timing matching the observed subevents (Fig. 4a,b); the rupture is delayed by asperity S3 causing an apparent slowdown in rupture speed and a drop in the moment-rate function; and the eventual break of asperity S3 generates a significant acceleration of the rupture front, the momentum of which extends the original rupture further out and produces a larger second peak in the moment-rate function (Fig. 4b,g, Extended Data Fig. 8 and Supplementary Video 2).

The modelling also illustrates that such fault asperities—or heterogeneity more broadly—may control the rupture propagation and seismic moment release. If the asperity that causes subevent S3 is removed from the model (model 2 in Fig. 4c,d,h and Supplementary Video 3), the moment release loses its two-peak shape and becomes smaller. If the asperity has altered friction properties that lower its peak resistance (see Methods for details), making it closer to the prestress level, the asperity no longer impedes the rupture, eliminating the observed delay in rupture speed and moment release (model 3 in Fig. 4e, f, i and Supplementary Video 4).

Implications for earthquake rupture study

This first application of DAS in earthquake rupture imaging, coupled with traditional low-frequency seismic analysis and dynamic rupture modelling, suggests a highly heterogeneous underlying fault with several prominent asperities that may control rupture dynamics. Such modulation of rupture behaviour by asperities may be ubiquitous as numerous other moderate-sized crustal earthquakes demonstrate similar or even longer duration and complex moment-release patterns in low-frequency observations (Extended Data Fig. 1), only a handful of which have been resolved by local dense arrays⁶. Although our study shows that a fault model with stronger asperities is fully consistent with the most prominent features of the high-frequency DAS back-projection as well as the low-frequency moment-rate release and finite-fault inversion of the investigated $M_{\rm w}$ 6.0 earthquake, it is possible that other physical mechanisms such as complex fault geometry, or a combination of factors, can provide an alternative explanation. Future work would be needed to examine all potential explanations by performing synthetic tests using dynamic simulations and/or joint inversion with seismic and geodetic data.

The DAS imaging produces a similar resolution to the dense Parkfield network of broadband seismometers at a much lower cost. With the extensive existing and proposed network of onshore telecommunication fibre cables¹² (for example, the California Middle-Mile Initiative³⁹; Fig. 1), DAS could provide a critical dataset for systematically investigating the rupture dynamics of moderate-sized and large crustal earthquakes. By combining such extensive datasets with data from conventional seismic networks and physics-based numerical modelling, we could form a unique insight into the role of geometrical, stress and material heterogeneities in earthquake ruptures.

Online content

Any methods, additional references, Nature Portfolio reporting summaries, source data, extended data, supplementary information, acknowledgements, peer review information; details of author contributions and competing interests; and statements of data and code availability are available at https://doi.org/10.1038/s41586-023-06227-w.

- Ishii, M., Shearer, P. M., Houston, H. & Vidale, J. E. Extent, duration and speed of the 2004 Sumatra-Andaman earthquake imaged by the Hi-Net array. Nature 435, 933-936 (2005).
- Simons, M. et al. The 2011 magnitude 9.0 Tohoku-oki earthquake: mosaicking the megathrust from seconds to centuries. Science 332, 1421-1425 (2011).
- Lay, T. et al. Depth-varying rupture properties of subduction zone megathrust faults. J. Geophys. Res. Solid Earth 117, B04311 (2012).
- Yao, H., Shearer, P. M. & Gerstoft, P. Compressive sensing of frequency-dependent seismic radiation from subduction zone megathrust ruptures. Proc. Natl Acad. Sci. USA 110, 4512-4517 (2013).
- Yin, J. & Denolle, M. A. The Earth's surface controls the depth-dependent seismic radiation of megathrust earthquakes, AGU Adv. 2, e2021AV000413 (2021).
- Allmann, B. P. & Shearer, P. M. A high-frequency secondary event during the 2004 Parkfield earthquake, Science 318, 1279-1283 (2007).
- Mesimeri, M., Zhang, H. & Pankow, K. L. Backprojection imaging of the 2020 M_w 5.5 Magna, Utah, earthquake using a local dense strong-motion network. Seismol. Res. Lett. 92, 640-646 (2020)
- Zhan, Z. Distributed acoustic sensing turns fiber-optic cables into sensitive seismic antennas. Seismol. Res. Lett. 91, 1-15 (2019).
- Lindsey, N. J. & Martin, E. R. Fiber-optic seismology. Annu. Rev. Earth Planet. Sci. 49, 309-336 (2021)
- Vallée, M., Charléty, J., Ferreira, A. M. G., Delouis, B. & Vergoz, J. SCARDEC: a new technique for the rapid determination of seismic moment magnitude, focal mechanism and source time functions for large earthquakes using body-wave deconvolution Geophys. J. Int. 184, 338-358 (2011)
- Goldberg, D. E., Koch, P., Melgar, D., Riquelme, S. & Yeck, W. L. Beyond the teleseism: introducing regional seismic and geodetic data into routine USGS finite-fault modeling. Seismol. Res. Lett. 93, 3308-3323 (2022).
- Ajo-Franklin, J. B. et al. Distributed acoustic sensing using dark fiber for near-surface characterization and broadband seismic event detection. Sci. Rep. 9, 1328 (2019).
- Xu. Y., Koper, K. D., Sufri, O., Zhu, L. & Hutko, A. R. Rupture imaging of the M., 7.9 12 May 2008 Wenchuan earthquake from back projection of teleseismic P waves. Geochem. Geophys. Geosyst. https://doi.org/10.1029/2008GC002335 (2009).
- Avouac, J.-P., Meng, L., Wei, S., Wang, T. & Ampuero, J.-P. Lower edge of locked main Himalayan Thrust unzipped by the 2015 Gorkha earthquake. Nat. Geosci. 8, 708-711 (2015).
- Fan, W. & Shearer, P. M. Detailed rupture imaging of the 25 April 2015 Nepal earthquake using teleseismic P waves, Geophys, Res, Lett. 42, 5744-5752 (2015)
- Meng, L., Inbal, A. & Ampuero, J.-P. A window into the complexity of the dynamic rupture of the 2011 M., 9 Tohoku-oki earthquake. Geophys. Res. Lett. https://doi.org/10.1029/ 2011GI 048118 (2011)
- Koper, K. D., Hutko, A. R., Lay, T. & Sufri, O. Imaging short-period seismic radiation from the 27 February 2010 Chile $M_{\rm w}$ 8.8 earthquake by back-projection of P, PP, and PKIKP waves. J. Geophys. Res. Solid Earth 117, B02308 (2012).
- Dodge, D. A., Beroza, G. C. & Ellsworth, W. L. Detailed observations of California foreshock sequences: implications for the earthquake initiation process. J. Geophys. Res. Solid Earth 101, 22371-22392 (1996).
- Dunham, E. M., Favreau, P. & Carlson, J. M. A supershear transition mechanism for cracks. Science 299, 1557-1559 (2003).
- Huang, Y., Meng, L. & Ampuero, J.-P. A dynamic model of the frequency-dependent rupture process of the 2011 Tohoku-oki earthquake. Earth Planets Space 64, 1 (2013).
- McLaskey, G. C. & Kilgore, B. D. Foreshocks during the nucleation of stick-slip instability. J. Geophys. Res. Solid Earth 118, 2982–2997 (2013).
- Schaal, N. & Lapusta, N. Microseismicity on patches of higher compression during larger-scale earthquake nucleation in a rate-and-state fault model. J. Geophys. Res. Solid Earth 124, 1962-1990 (2019).
- Ellsworth, W. L. & Beroza, G. C. Seismic evidence for an earthquake nucleation phase. Science 268, 851-855 (1995).
- Kilb, D. & Gomberg, J. The initial subevent of the 1994 Northridge, California, earthquake: is earthquake size predictable? J. Seismol. 3, 409-420 (1999).

- Ide, S. Frequent observations of identical onsets of large and small earthquakes. Nature **573**, 112-116 (2019).
- Meier, M.-A., Ampuero, J.-P., Cochran, E. & Page, M. Apparent earthquake rupture predictability. Geophys. J. Int. 225, 657-663 (2020).
- Ross, Z. E. et al. Hierarchical interlocked orthogonal faulting in the 2019 Ridgecrest earthquake sequence. Science 366, 346-351 (2019).
- Zheng, A., Chen, X. & Xu, W. Present-day deformation mechanism of the northeastern Mina deflection revealed by the 2020 $M_{\rm w}$ 6.5 Monte Cristo Range earthquake. Geophys. Res. Lett. 47, e2020GL090142 (2020).
- 29. Pierce, I. K. D. et al. Accommodation of plate motion in an incipient strike-slip system: the Central Walker Lane. Tectonics 40, e2019TC005612 (2021).
- 30. Pollitz, F. F., Wicks, C. W. & Hammond, W. C. Kinematic slip model of the 2021 M 6.0 Antelope Valley, California, earthquake. Seismic Rec. 2, 20-28 (2022).
- $Yin, J., Li, Z.\ \&\ Denolle, M.\ A.\ Source\ time\ function\ clustering\ reveals\ patterns\ in\ earthquake$ dynamics. Seismol. Res. Lett. 92, 2343-2353 (2021).
- 32. Kiser, E. & Ishii, M. Back-projection imaging of earthquakes, Annu. Rev. Earth Planet, Sci. 45. 271-299 (2017).
- Yagi, Y., Nakao, A. & Kasahara, A. Smooth and rapid slip near the Japan Trench during the 33. 2011 Tohoku-oki earthquake revealed by a hybrid back-projection method. Earth Planet. Sci. Lett. 355-356, 94-101 (2012).
- 34. Madariaga, R. High frequency radiation from dynamic earthquake. Ann. Geophys. 1, 17 (1983).
- Li, B. et al. Rupture heterogeneity and directivity effects in back-projection analysis. J. Geophys. Res. Solid Earth 127, e2021JB022663 (2022).

- Sagy, A., Brodsky, E. E. & Axen, G. J. Evolution of fault-surface roughness with slip Geology 35, 283-286 (2007).
- 37. Dunham, E. M., Belanger, D., Cong, L. & Kozdon, J. E. Earthquake ruptures with strongly rate-weakening friction and off-fault plasticity, part 2: nonplanar faults. Bull. Seismol. Soc. Am. 101, 2308-2322 (2011).
- 38. Lapusta, N. & Liu, Y. Three-dimensional boundary integral modeling of spontaneous earthquake sequences and aseismic slip. J. Geophys. Res. Solid Earth https://doi.org/ 10.1029/2008JB005934 (2009).
- California Department of Technology. Statewide Middle-Mile Analysis. https://middle-milebroadband-initiative.cdt.ca.gov/pages/data-and-analysis (2022).
- 40. Lee, E.-J. et al. Full-3-D tomography for crustal structure in Southern California based on the scattering-integral and the adjoint-wavefield methods. J. Geophys. Res. Solid Earth 119, 6421-6451 (2014).

Publisher's note Springer Nature remains neutral with regard to jurisdictional claims in published maps and institutional affiliations.

Springer Nature or its licensor (e.g. a society or other partner) holds exclusive rights to this article under a publishing agreement with the author(s) or other rightsholder(s); author self-archiving of the accepted manuscript version of this article is solely governed by the terms of such publishing agreement and applicable law.

© The Author(s), under exclusive licence to Springer Nature Limited 2023

Methods

Back-projection with P and S phases

Traditional back-projection imaging uses only teleseismic P waves to identify high-frequency radiators from large earthquakes. The teleseismic S waves are not used owing to their strong attenuation at relevant high frequencies. Teleseismic P-wave back-projection imaging has no depth resolution as the ray paths for teleseismic P waves are almost vertical in the source region, which results in an unresolvable trade-off between the origin time and depth. Thus, teleseismic P-wave back-projection imaging is performed on a two-dimensional horizontal plane and its depth interpretation relies purely on its projection onto a pre-known fault plane.

For our case of a regional-distance DAS array with respect to the moderate-sized earthquake, both P and S phases retain clear signals at frequencies higher than 1 Hz, and they are well separated. We take advantage of both phases to obtain a 3D back-projection image that has depth resolution. To accommodate waveform complexities caused by heterogeneous crustal structures, we use waveforms from nearby aftershocks—which are approximately 3 km away from the mainshock's epicentre according to the USGS catalogue—instead of the Dirac delta function in traditional teleseismic back-projection—as our EGFs. We denote by $g_j(t)$ the EGF waveform from an aftershock recorded at channel j, with t representing time. We select the EGF to be 2-s long for the P phase and 4-s long for the S phase. We then separately cross-correlate them with the continuous recording $d_j(t)$ of the mainshock to obtain the P and S correlograms:

$$c_j^X(t) = \langle d_j(t), g_j^X(t) \rangle, \tag{1}$$

where the angle brackets represent the cross-correlation operator, and superscript X represents either the P or the S phase.

We back-project the P and S correlograms to the mainshock source region through their corresponding one-dimensional velocity models (Extended Data Fig. 5). For each location \mathbf{i} in the 3D back-projection region, the stacked average correlation $s(\mathbf{i}, t)$ is:

$$s(\mathbf{i},t) = \frac{1}{2N} \sum_{j=1}^{N} \{ c_{j}^{P}(t+\tau_{\mathbf{i}j}^{P}) + c_{j}^{S}(t+\tau_{\mathbf{i}j}^{S}) \},$$
 (2)

where τ_{ij}^P and τ_{ij}^S denote the modelled P and S travel times from location i to channel j, and N is the number of channels used.

At the real source location \mathbf{i}_0 in the 3D back-projection volume and the correct origin time t_0 , we have:

$$s(\mathbf{i_0}, t_0) = \frac{1}{2N} \sum_{j=1}^{N} \{ c_j^{\mathsf{P}}(t_0 + \tau_{\mathbf{i_0}j}^{\mathsf{P}}) + c_j^{\mathsf{S}}(t_0 + \tau_{\mathbf{i_0}j}^{\mathsf{S}}) \}, \tag{3}$$

where $\tau^P_{i_0j}$ and $\tau^S_{i_0j}$ represent the modelled P and S travel times from the real source location i_0 to channel j. The stacked cross-correlation in equation (3) is then maximized as the cross-correlation reaches the maximum at the theoretical arrival time at each channel for both P and S phases. As the cross-correlation is with respect to the EGF, the location of the imaged subevents is relative to the location of the aftershock that serves as the EGF.

To visualize the location of subevents and temporal change of the four-dimensional back-projection volume, we use time-dimension slices. Conventional back-projection uses a constant-time slice for all the grids and often suffers from the 'swimming artefact', in which the stacked energy appears to propagate towards the azimuthal-limited array owing to the trade-off between travel time and travel distance ^{13,41}. To mitigate this artefact, we define a 'slowness time slice' on which the time for the *i*th grid is adjusted according to their P-wave travel times τ^P_{ir} from the reference receiver r (0th channel location) (equation (4)). This approach is similar to the 'reference time window' strategy⁴¹ but

applied in the time domain. We illustrate how this approach could alleviate the ambiguity in interpreting subevents in Extended Data Fig. 2f.

image
$$(\mathbf{i}, t_{\text{image}}) = s(\mathbf{i}, t - \tau_{\mathbf{i}r}^{P}),$$
 (4)

Using two aftershock events for EGF

We start by using the waveforms of a local magnitude (M_1) 3.7 aftershock (event ID NC73585056) as our EGF. We bandpass filter (1–5 Hz) the seismic recordings for both aftershock and mainshock and then cross-correlate their waveforms channel by channel. The resulting S correlograms show three approximately aligned correlation peaks across all channels, after being shifted by travel times from the catalogue hypocentre (Extended Data Fig. 2b). In the P correlograms (Extended Data Fig. 2a), the correlation peaks after the first peak do not stand out: this is probably caused by the radiation pattern, as the DAS array samples near the P nodal plane of the mainshock. With direct P being weak, the coda waves are more prominent and contribute significantly to the individual P correlogram. Therefore, it is critical to stack P and S correlograms over all the channels to identify the subevents (Extended Data Fig. 4). The stacked correlograms show three distinct peaks that correspond to three subevents S1-S3 (Extended Data Figs. 4b-d). As we increase the upper limit of the frequency band from 5 Hz to 8 Hz, an earlier correlation peak (Extended Data Fig. 2d) emerges ahead of the most distinct peak (Extended Data Fig. 4b). To confirm this SO subevent, we use an M_w 4.2 aftershock (event ID NC73585086) as another EGF. The subevent S0 correlation peak stands out as the highest correlation at a frequency band of 4-8 Hz and corresponds to subevent SO (Extended Data Fig. 4a). The higher-frequency band captures the high-frequency first break, which coincides with the initial break used by the local network to determine the origin time of the $M_{\rm w}$ 6.0 event.

In the EGF method, ideally, the EGFs should be identical to the true Green's function, which would require the EGF event to be simple in rupture and have the same location and focal mechanism as the mainshock. In practice, the EGFs may be slightly different from the true Green's function and from each other owing to rupture complexity and small differences in location, focal mechanism and duration. The two EGFs we select are similar to each other (Extended Data Fig. 2e), especially at lower frequencies, but still have small differences at higher frequencies. The differences are expected and may explain the different sensitivity to different parts of the mainshock rupture. For example, it seems that the second EGF event shares a more similar focal mechanism to subevent SO and hence can resolve it better than the first EGF.

Scaling relationship for estimating subevents' magnitudes

To estimate the magnitudes of subevents, we assume that the distinct peaks recorded on the tangential components of strong-motion stations (Fig. 3c) represent the S arrival from individual subevents. The approximate subevent magnitudes could then be inferred empirically from their peak amplitudes 42 . We derive an empirical linear relationship between earthquake magnitudes (M, taken from the catalogue), log-scale peak velocity amplitudes ($P_{\rm v}$ in m s $^{-1}$ on the tangential component), log-scale epicentral distances (R in km) and site responses (C) using hundreds of aftershocks at five strong-motion stations (Fig. 1):

$$M = a\log_{10}(P_{v}) + b\log_{10}(R) + C \text{ (station)}.$$
 (5)

Using 358 aftershocks that have magnitudes ranging from 2 to 5 near the mainshock, the regression coefficients are determined as a = 1.01 and b = 1.39, and the site terms at the five strong-motion stations are C(SJC) = 5.0, C(EBPB) = 5.2, C(65654) = 5.2, C(QNBC) = 4.4 and C(WILB) = 5.3.

On the basis of this regression relationship, we calculate the approximate magnitude for each subevent given the epicentral distance and

individual peak velocity amplitude measured on the tangential components of strong-motion stations (Extended Data Fig. 3i).

Subevent detection significance

Intuitively, the back-projection imaging quality and robustness would improve as we increase the number of stacking stations and channels as the signal would stack coherently whereas the noise would cancel out. To quantitatively demonstrate the improvement of back-projection imaging with the increasing number of stations and channels and to compare the imaging robustness of DAS systems with conventional stations, we define the detection significance (*MAD)⁴³ as the ratio between the maximum cross-correlation max(s) minus median cross-correlation median(s) and the median absolute deviation (MAD):

*MAD =
$$\frac{\max(s) - \text{median}(s)}{\text{MAD}}$$
, (6)

with MAD defined as:

$$MAD = median(|s - median(s)|).$$
 (7)

Here, s represents the stacked correlograms in equation (4) at the imaged subevent location. A higher *MAD represents a more robust imaging result that stands out from the background noise.

In Extended Data Fig. 7e, we perform bootstrapping for DAS back-projection imaging by randomly selecting different numbers of channels used in back-projection. The *MAD increases almost linearly with the increasing number of channels used on a log scale. The *MAD for DAS is about five times as large as that of conventional stations.

Subevents versus depth phases

Previous studies have shown that depth phases can cause artefacts that may be falsely interpreted as subevents⁴⁴. We exclude the possibility of depth phases causing the observed correlation peaks based on the following argument: if the correlation peaks are caused by the depth phases, we would see similar correlation peak patterns for aftershocks with similar depth. However, these multiple correlation peaks are not observed for such aftershocks (Extended Data Fig. 2c). We thus conclude that the trailing correlation peaks are not caused by depth phases but rather correspond to energetic sources as the rupture evolves.

Dynamic rupture modelling

Our simulations consider the slip on a two-dimensional fault embedded into a 3D uniform, isotropic and elastic medium. To conduct simulations of dynamic rupture, we utilize a spectral boundary integral method³⁸, which solves the evolution of slip rate and other variables along the fault by equating the evolving fault shear stress to its shear resistance. The evolution of shear stress on each discretized cell of the fault depends, in part, on slip elsewhere on the fault through wave-mediated dynamic stress transfers which, in part, depend on the bulk properties. We assign typical rock properties to the bulk (Extended Data Table 1a).

The shear resistance along the fault follows the laboratory-derived Dieterich-Ruina rate-and-state friction law with the state evolution governed by the ageing formulation⁴⁵⁻⁴⁷:

$$\tau = \sigma f(V, \theta) = \sigma \left[f_* + a \ln \frac{V}{V_*} + b \ln \frac{V_* \theta}{D_{RS}} \right], \tag{8}$$

$$\dot{\theta} = 1 - \frac{V\theta}{D_{\rm ps}},\tag{9}$$

where τ is the shear resistance, σ is the normal stress, f is the rate-state friction coefficient at sliding rate V and state variable θ , f is the reference steady-state friction coefficient at reference sliding rate V_{*} , D_{RS} is the characteristic slip distance, and a and b are the direct effect and evolution effect parameters, respectively. We use the version of the expressions (8) and (9) regularized for zero and negative slip rates⁴⁸. Dynamic slip can nucleate only if the region with velocity-weakening friction properties, (a-b) < 0, is larger than the nucleation size h_{RA}^* which can be estimated by 49,50:

$$h_{\rm RA}^* = \frac{\pi}{2} \frac{\mu b D_{\rm RS}}{(b-a)^2 \sigma},\tag{10}$$

where μ is the shear modulus. We choose our spatial discretization to resolve both this nucleation length scale as well as the rapid evolution of shear resistance and slip rate at the rupture front that occurs over the spatial length scale—the cohesive-like zone—which can be estimated as 38,51,52:

$$\Lambda_0 = C_1 \frac{\mu^*}{M},\tag{11}$$

where $C_1 = \frac{9\pi}{32}$ is a constant and $W = \frac{b\sigma}{D_{RS}}$ is the weakening rate. Our simulation methodology allows us to resolve earthquake sequences in their entirety, including spontaneous nucleation, dynamic rupture propagation, postseismic slip and interseismic creep³⁸. However, here we use it to simulate a single instance of nucleation and dynamic rupture propagation on a fault segment with velocity-weakening steady-state properties of rate-and-state friction, with the initial conditions motivated by earthquake sequence simulations in models with similar fault properties. The initial conditions are then further tuned to produce the observed slip distribution.

Adjustable parameters in the model include the rate-and-state properties of the fault $(f_*, a, b \text{ and } D_{RS})$, the initial conditions, and the size and properties of the asperities. We tune these parameters simultaneously to fit the observed moment rate, duration of rupture, magnitude and occurrence times of the individual subevents, assisted by known relationships between frictional properties and the resulting rupture dynamics in prior modelling^{22,38,53}. The relative locations of the asperities, which are modelled as areas of higher effective normal stress (Extended Data Table 1b and Extended Data Fig. 9), correspond exactly to the correlation peaks of the back-projection (Fig. 3) with only minor differences for subevent S3 within the range of high correlation to match its occurrence time.

The initial shear-stress level is assigned with respect to τ_{dyn} , the dynamic shear resistance to which a given point on the fault converges as the rupture propagates through it, given by the steady-state shear resistance at a dynamic slip rate, V_{dyn} :

$$\tau_{\rm dyn} = \sigma \left[f_* + (a - b) \ln \frac{V_{\rm dyn}}{V_*} \right]. \tag{12}$$

To select the initial stresses, $V_{\rm dyn}$ is approximated to be 0.1 m s⁻¹. The sustained slip rate values behind the rupture front vary from that to several metres per second, but the exact value of $V_{\rm dyn}$ does not change $\tau_{\rm dvn}$ much owing to the natural log. Initial stress levels sufficiently above $\tau_{\rm dvn}$ present favourable conditions for rupture propagation, as they allow for positive stress drop. Initial stress levels below $\tau_{\rm dyn}$ present unfavourable conditions for rupture propagation. Thus, the shear stress level is prescribed to be above τ_{dvn} over the desired rupture region and to decrease towards its edges, with the boundary of the contour where the initial shear stress equals τ_{dyn} motivated by the USGS finite-fault inversion (Fig. 3). On the basis of long-term simulations, the initial stress level is chosen to be at maximum 1.5 MPa above the local $\tau_{\rm dyn}$ near the nucleating region. The state variable is prescribed similarly to create a region of low θ near the nucleating region that increases gradually to a uniform value of 50 years. Given fault healing in the interseismic period with θ growing with the time⁵⁴, as implied by the formulations (8) and (9), this serves as an appropriate initial condition for the region

of the Antelope Valley earthquake that has not recorded an event at the scale of $M_{\rm w}$ 6.0 for at least such time. Once the shear stress and θ are prescribed, the slip rate is uniquely defined by equation (8), resulting in a region of slow, rupture-nucleating slip rate in the nucleation region (about $10^{-7}~{\rm m\,s^{-1}}$) that decreases monotonically to a much lower rate, mimicking a locked fault on the interseismic timescales (about $10^{-17}~{\rm m\,s^{-1}}$, which would correspond to slip of less than a nanometre in a year).

Initial conditions and frictional properties of the asperities are configured in conjunction with the given properties of the background fault to match the observed data (Extended Data Table 1b). The size and level of initial shear stress above $\tau_{\rm dyn}$ of the asperities are selected so that the event reproduces the observed moment magnitude, as the static stress drop increases with larger initial stress and, in turn, it is proportional to slip and the amount of moment released from breaking the asperities. The asperity sizes are chosen to be smaller than the local nucleation size of the asperity given their higher normal stress, to mimic conditions that would promote the build-up of shear stress on the asperities during interseismic loading without nucleating dynamic slip. The relative differences in the sizes of the asperities are chosen to reflect the differences in the magnitudes of the subevents inferred from the scaling analysis (Extended Data Fig. 6).

The initial conditions and frictional parameters of the asperities are further tuned to illustrate how they can either impede or promote the rupture, to achieve the desired fit to the moment-release rate in time (Extended Data Fig. 9 and Extended Data Table 1). To understand how such properties could be selected systematically, it is useful to consider the friction-displacement curve of a single point on the fault as the rupture passes through it. At the dynamic rupture front, the rate-and-state formulation yields an evolution of shear stress closely mimicking the linear slip-weakening law^{38,55}. Under these conditions, the initial friction, $\left(\frac{\tau}{\sigma}\right)_{\text{ini}}$, peak friction, $\left(\frac{\tau}{\sigma}\right)_{\text{peak}}$, dynamic friction, $\left(\frac{\tau}{\sigma}\right)_{\text{dyn}}$, and slope of the weakening curve, W, are given by:

$$\left(\frac{\tau}{\sigma}\right)_{\text{ini}} = f_* + a \ln\left(\frac{V_{\text{ini}}}{V_*}\right) + b \ln\left(\frac{\theta_{\text{ini}}}{\theta_*}\right)$$

$$\left(\frac{\tau}{\sigma}\right)_{\text{peak}} = f_* + a \ln\left(\frac{V_{\text{dyn}}}{V_*}\right) + b \ln\left(\frac{\theta_{\text{ini}}}{\theta_*}\right)$$

$$\left(\frac{\tau}{\sigma}\right)_{\text{dyn}} = f_* + a \ln\left(\frac{V_{\text{dyn}}}{V_*}\right) + b \ln\left(\frac{\theta_{\text{dyn}}}{\theta_*}\right)$$

$$W = \frac{b}{D_{\text{RS}}}$$
(13)

where the subscript 'ini' represents initial conditions and $\theta_* = \frac{D_{RS}}{V_*}$. The expression for the peak friction is an approximation that assumes that the peak friction is reached with negligible slip such that no evolution of the state variable has occurred; simulations show that this is a good assumption at the rupture tip. To break the asperity, the incoming rupture has to dynamically supply the stress needed to make up the difference between the initial and peak friction, $\Delta \left(\frac{\tau}{\sigma}\right)_{st'}$ given by:

$$\left(\frac{\tau}{\sigma}\right)_{\text{peak}} - \left(\frac{\tau}{\sigma}\right)_{\text{ini}} \equiv \Delta\left(\frac{\tau}{\sigma}\right)_{\text{df}} = a \ln\left(\frac{V_{\text{dyn}}}{V_{\text{ini}}}\right),\tag{14}$$

This relation shows that a lower initial slip rate $V_{\rm ini}$ or higher value of the rate-and-state parameter a both increase the asperity distance to failure, increasing the amount of dynamic loading it requires to rupture. Making $\Delta \left(\frac{\tau}{\sigma}\right)_{\rm df}$ large enough can temporarily stall the rupture, with dynamic slip surrounding the asperity and loading it to the needed peak stress. Increasing a also has the compounding effect of increasing the nucleation size of the asperity, making it more inherently stable and unfavourable for dynamic rupture. Such an effect on the nucleation size could also be achieved by increasing $D_{\rm RS}$, independent of changes

to $\Delta\left(\frac{\tau}{\sigma}\right)_{\mathrm{df}}$. An increase in D_{RS} would also reduce the weakening rate W post-peak, another unfavourable factor for dynamic rupture. On the flip side, the tendency of the asperity to further promote the rupture can be enhanced by increasing $\left(\frac{\tau}{\sigma}\right)_{\mathrm{ini}}$. This would both decrease $\Delta\left(\frac{\tau}{\sigma}\right)_{\mathrm{df}}$ promoting the initial breakage of the asperity and increase the dynamic and static stress drop on the asperity, giving the rupture a bigger push. Increasing the weakening rate W, by increasing b and/or decreasing b would make the rupture more dynamic as well as would additionally decrease the nucleation size of the asperity, making it more inherently unstable and favourable for dynamic rupture.

The three models discussed in the main text (Fig. 4) highlight some of these effects by modifying the properties of the fourth asperity that leads to subevent S3. In model 1, the asperity has higher a and lower V_{ini} than the surroundings, allowing it to initially impede the rupture (Fig. 4g) compared with model 2 with no fourth asperity (Fig. 4h) and model 3 which has a lower value of a at the asperity (Fig. 4i). This manifests in the apparent low rupture speed between subevents SO and S3 in model 1. When the fourth asperity ruptures in subevent S3 in model 1, the moment released results in the second larger peak of the moment-rate function (Fig. 4b); this peak is largely absent in model 2 with no asperity (Fig. 4d). The rupture delay at the asperity in model 1 also produces the temporary dip in the overall moment-release rate as observed for the natural event; this dip is absent in model 3 with lower a and hence lower peak resistance of the asperity (Fig. 4f). The choices of the modelling parameters are non-unique; the effects illustrated by the modelling and the match to observations can be achieved by other combinations of background fault and asperity parameters and initial conditions. A systematic exploration of the effects of asperities on rupture subevents and overall rupture, for both single rupture events and in the context of earthquake sequences, will be a topic of future work.

Data availability

Seismic data at conventional stations are from the Northern California Earthquake Data Center. The DAS recordings of the mainshock and the aftershocks used for the empirical Green's functions are available from Caltech Data at https://doi.org/10.22002/7h65h-89163.

Code availability

The code for processing the DAS data and performing back-projection is also available at https://doi.org/10.22002/7h65h-89163.

- Meng, L., Ampuero, J.-P., Luo, Y., Wu, W. & Ni, S. Mitigating artifacts in back-projection source imaging with implications for frequency-dependent properties of the Tohoku-oki earthquake. Earth Planets Space 64, 1101–1109 (2012).
- Wurman, G., Allen, R. M. & Lombard, P. Toward earthquake early warning in northern California. J. Geophys. Res. Solid Farth https://doi.org/10.1029/2006.JB004830 (2007).
- Li, Z. et al. Rapid response to the 2019 Ridgecrest earthquake with distributed acoustic sensing. AGI Adv. 2. e2021AV000395 (2021).
- Yao, H., Shearer, P. M. & Gerstoft, P. Subevent location and rupture imaging using iterative backprojection for the 2011 Tohoku M_w 9.0 earthquake. Geophys. J. Int. 190, 1152–1168 (2012).
- Dieterich, J. H. Modeling of rock friction: 1. Experimental results and constitutive equations. J. Geophys. Res. Solid Earth 84, 2161–2168 (1979).
- Ruina, A. Slip instability and state variable friction laws. J. Geophys. Res. Solid Earth 88, 10359–10370 (1983).
- Marone, C. Laboratory-derived friction laws and their application to seismic faulting Annu. Rev. Earth Planet. Sci. 26, 643–696 (1998).
- Noda, H. & Lapusta, N. Three-dimensional earthquake sequence simulations with evolving temperature and pore pressure due to shear heating: effect of heterogeneous hydraulic diffusivity. J. Geophys. Res. Solid Earth 115, B12314 (2010).
- Rubin, A. M. & Ampuero, J.-P. Earthquake nucleation on (aging) rate and state faults. J. Geophys. Res. Solid Earth https://doi.org/10.1029/2005JB003686 (2005).
- Chen, T. & Lapusta, N. Scaling of small repeating earthquakes explained by interaction of seismic and aseismic slip in a rate and state fault model. J. Geophys. Res. Solid Earth https://doi.org/10.1029/2008JB005749 (2009).
- Palmer, A. C., Rice, J. R. & Hill, R. The growth of slip surfaces in the progressive failure of over-consolidated clay. Proc. R. Soc. Lond. A 332, 527–548 (1973).
- Day, S. M., Dalguer, L. A., Lapusta, N. & Liu, Y. Comparison of finite difference and boundary integral solutions to three-dimensional spontaneous rupture. J. Geophys. Res. Solid Earth https://doi.org/10.1029/2005JB003813 (2005).

- Barbot, S., Lapusta, N. & Avouac, J.-P. Under the hood of the earthquake machine: toward predictive modeling of the seismic cycle. Science 336, 707–710 (2012).
- Dieterich, J. H. & Kilgore, B. D. Direct observation of frictional contacts: new insights for state-dependent properties. Pure Appl. Geophys. 143, 283–302 (1994).
- Bizzarri, A. & Cocco, M. Slip-weakening behavior during the propagation of dynamic ruptures obeying rate- and state-dependent friction laws. J. Geophys. Res. Solid Earth https://doi.org/10.1029/2002JB002198 (2003).

Acknowledgements This work is supported by the US National Science Foundation (NSF) (EAR-1848166 and EAR-1724686), United States Geological Survey (G23AP00111 and G21AP10037), the Gordon and Betty Moore Foundation, and the Southern California Earthquake Center (SCEC). This is SCEC contribution 12737. We thank E. Williams for performing the tap test; J. Yin, Z. Jia, W. Wu and Y. Zhang for discussions; and M. T. Ort and the California Broadband Cooperative for providing fibre access for this study.

Author contributions J.L. and Z.Z. designed the work. J.L. performed the back-projection imaging. T.K. and N.L. designed the rupture modelling. T.K. performed the rupture simulations. J.L. and E.B. implemented the processing code. J.L., Z.Z., T.K. and N.L. prepared and revised the paper. E.B. collected the DAS data and determined the fibre channel locations.

Competing interests The authors declare no competing interests.

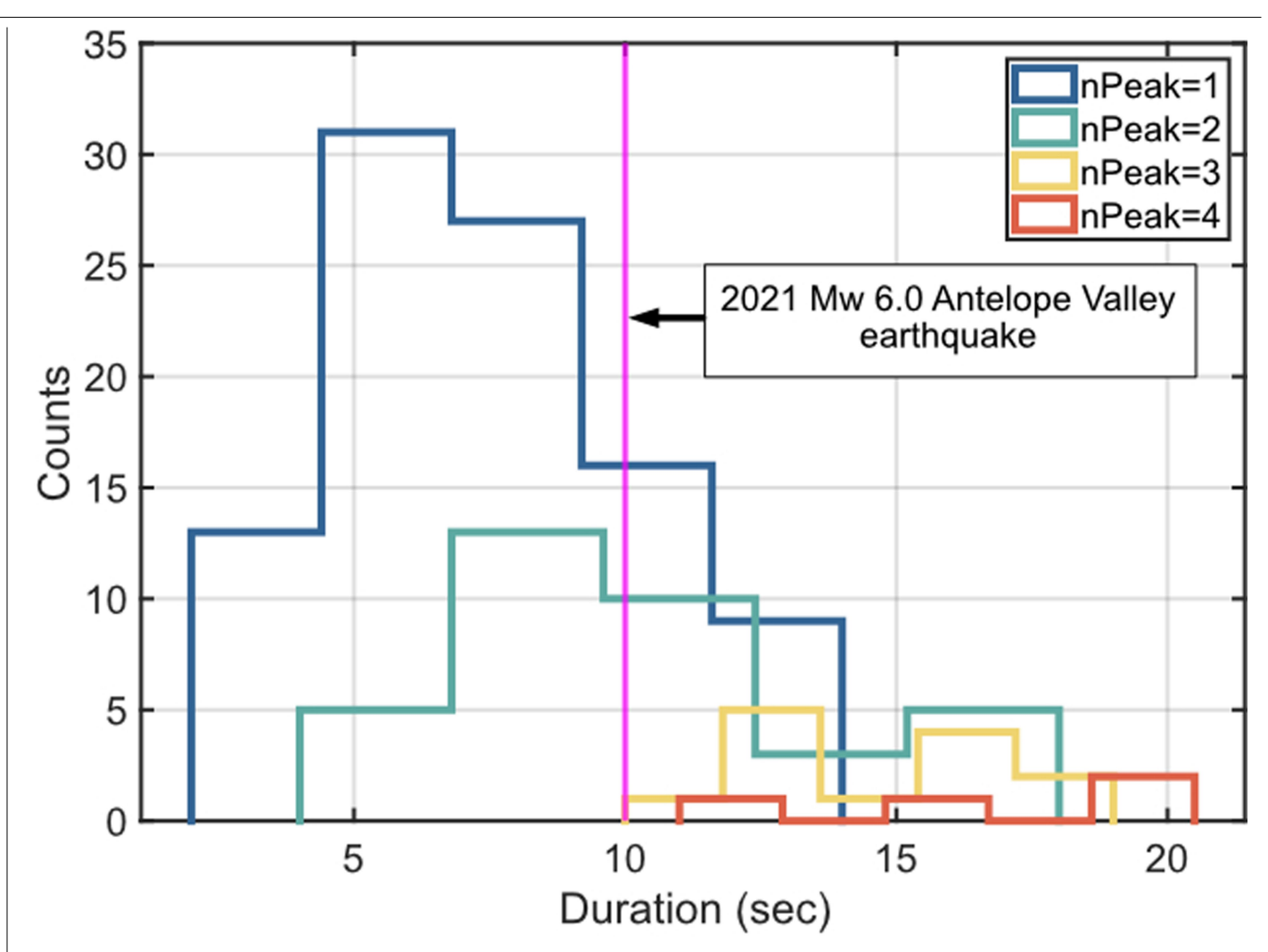
Additional information

 $\textbf{Supplementary information} \ The online version contains supplementary material available at \ https://doi.org/10.1038/s41586-023-06227-w.$

Correspondence and requests for materials should be addressed to Jiaxuan Li.

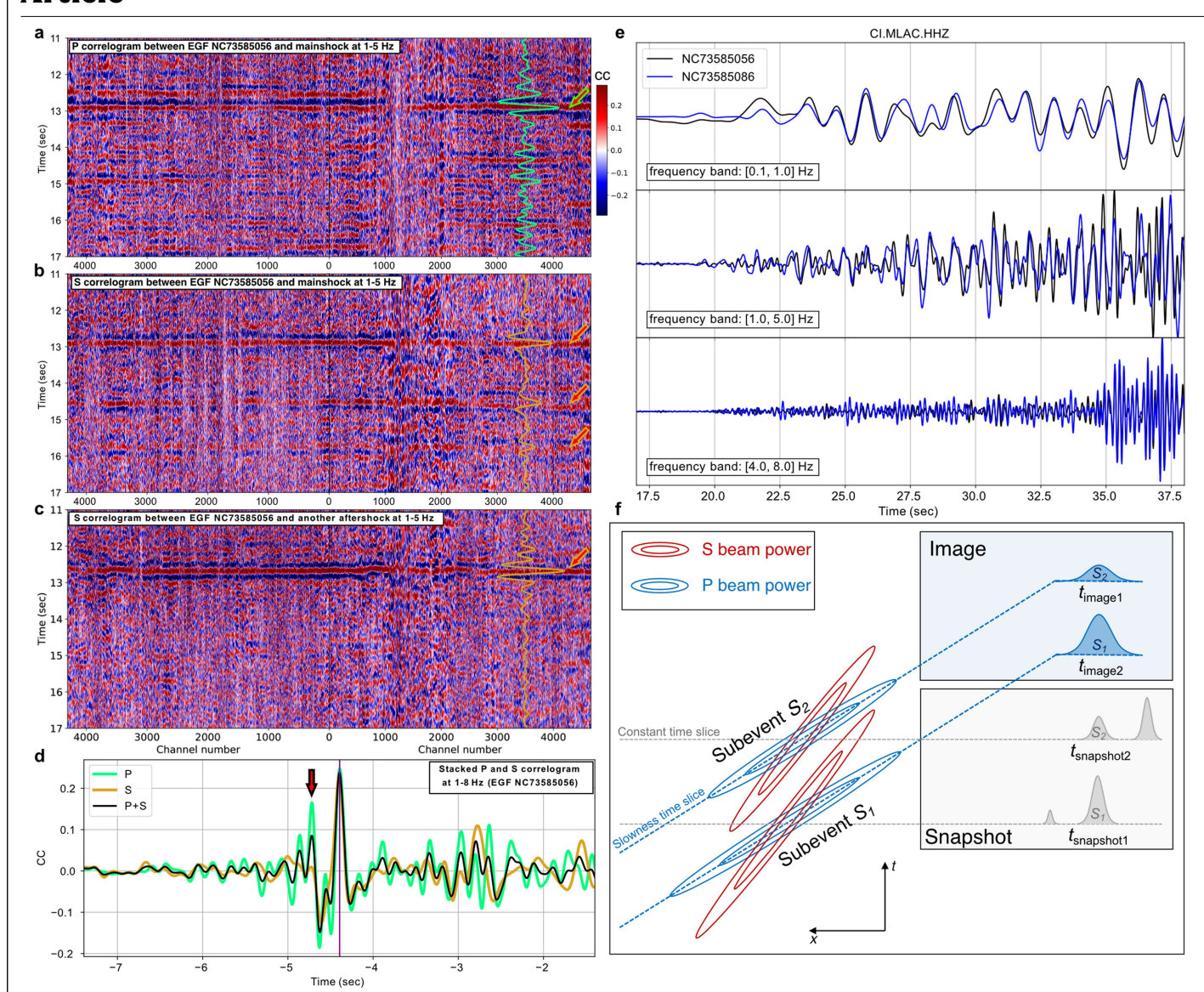
Peer review information Nature thanks Martijn van den Ende and Deborah Kilb for their contribution to the peer review of this work.

Reprints and permissions information is available at http://www.nature.com/reprints.



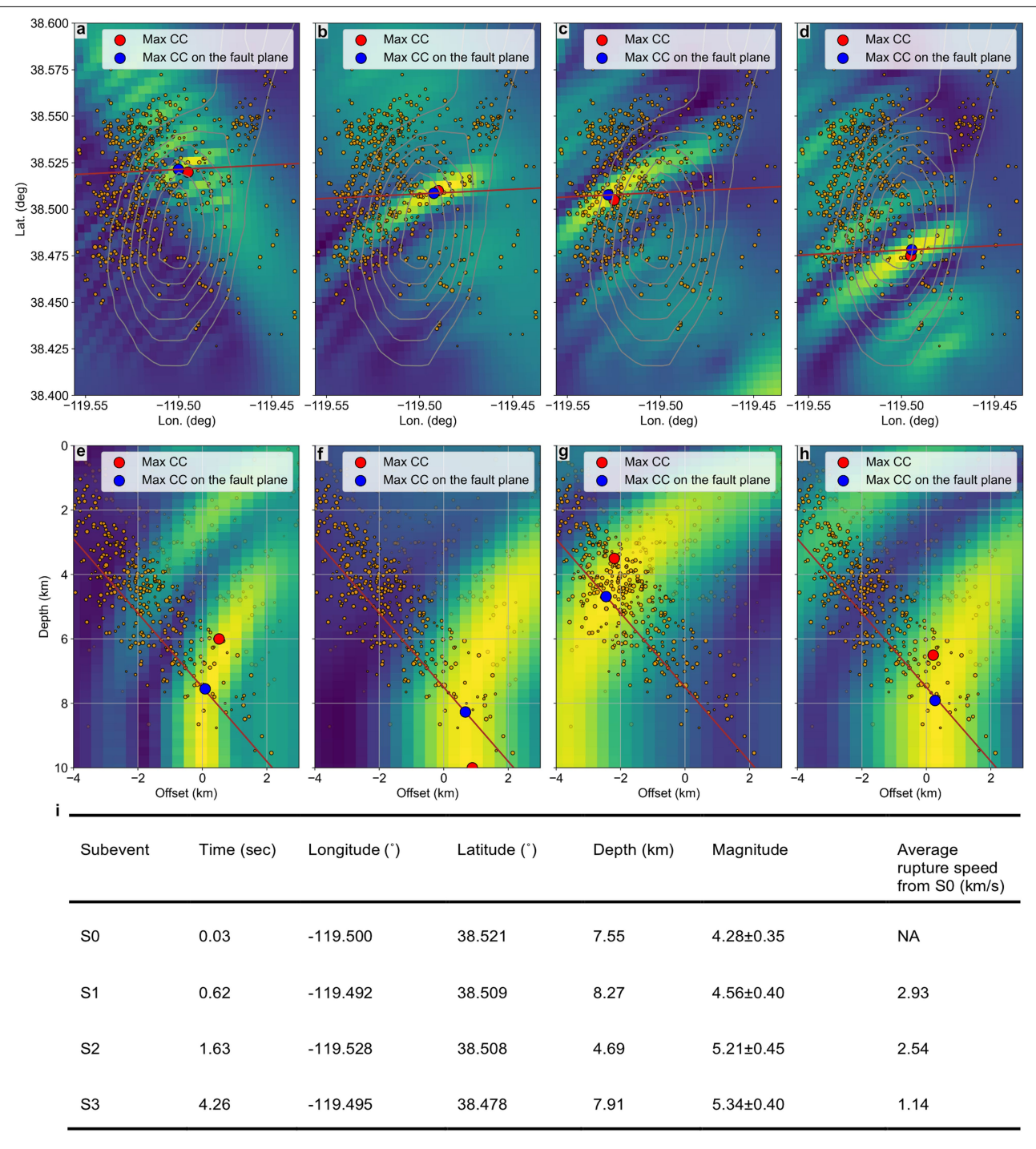
Extended Data Fig. 1| Histograms of source duration for similar earthquakes. We select earthquakes with magnitudes between 5.9 and 6.1 and depths within 5–10 km from the SCARDEC database 10,11 . Four colored histograms represent the duration distribution for earthquakes with different numbers of peaks in

their moment-rate function. The vertical magenta line represents the approximate source duration of the 2021 Mw 6.0 Antelope Valley earthquake inferred from the SCARDEC average moment rate function $^{10}. \\$



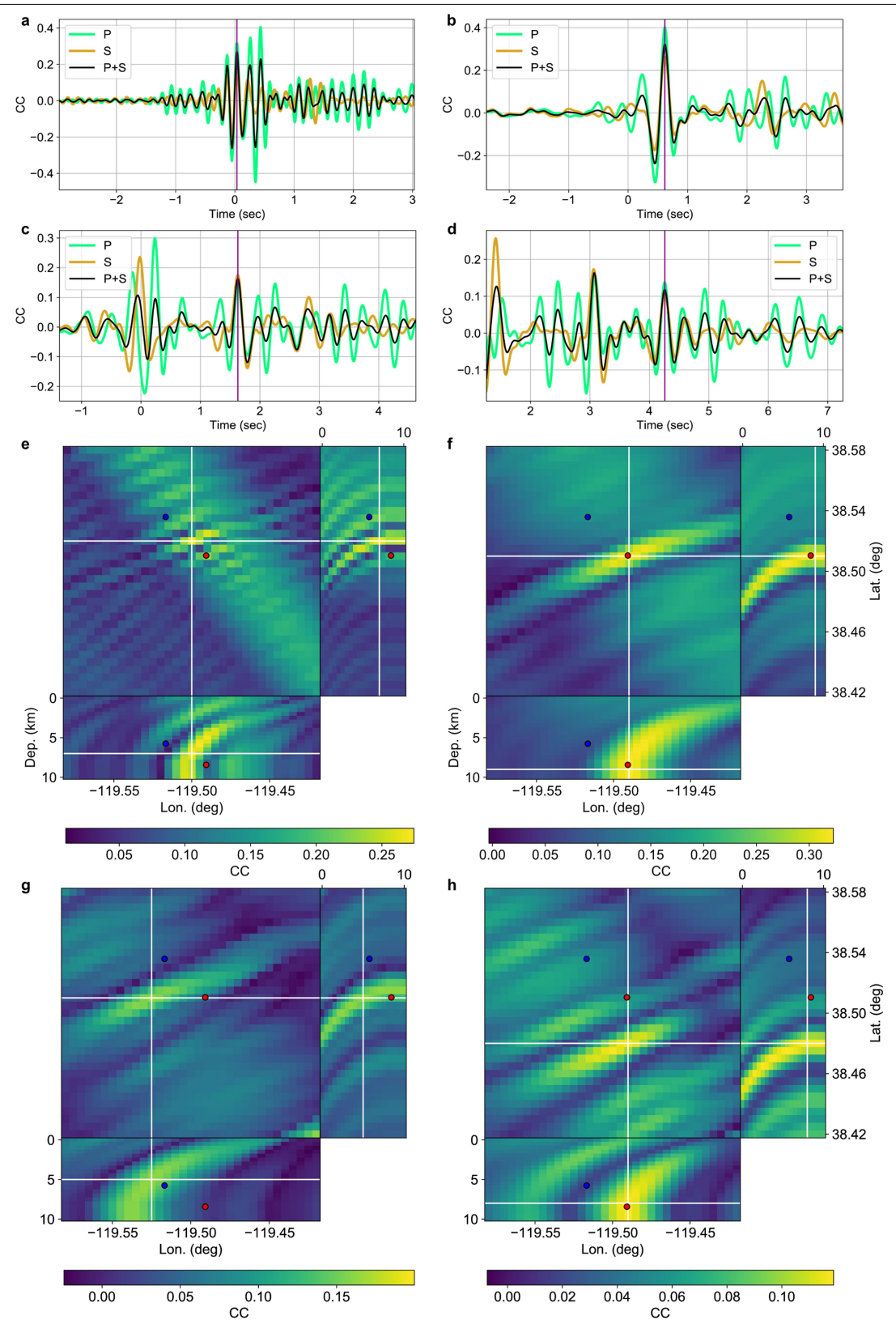
Extended Data Fig. 2 | Example correlograms and illustration of our back-projection imaging. a, b, P- and S-phase correlograms of the Mw 6.0 mainshock calculated by cross-correlating the mainshock waveform with the EGFs from the aftershock (event ID: NC73585056) at a frequency band of 1–5 Hz, with noticeable correlation peaks across all channels marked by arrows. For both phases, each channel has been time-shifted by the corresponding phase travel time from the mainshock epicenter in the catalog. In the P correlogram, the correlation peaks after the first peak do not stand out. This is likely caused by the radiation pattern, since the DAS array samples close to the P nodal line. The coda waves are more prominent and contribute more to the individual P correlogram. c, S-phase correlograms of an Mw 4.5 aftershock (event ID: NC73585291) that has a similar depth and focal mechanism to the mainshock using the same EGF. Unlike the complicated S-phase correlogram for the mainshock in b, this correlogram shows only one horizontally aligned

correlation peak, indicating a simpler rupture process. ${\bf d}$, When we increase the frequency band to 1–8 Hz and stack the correlograms using the same EGF, another correlation peak (indicated by the red arrow) emerges before the highest correlation peak. This correlation peak is further enhanced using another EGF (event ID: NC73585086) (Extended Data Fig. 4a). ${\bf e}$, Normalized vertical-component recordings of both EGF events on a closeby broadband station show their similarities at different frequency bands. ${\bf f}$, Schematic diagram of back-projection imaging using both P and S phases. The P and S beam power (blue and red contours, respectively) have different slopes due to their differences in slowness. Therefore, joint P and S back-projection helps to reduce the distance-time trade-off. We adopt a "slowness time slice" (blue dashed line) instead of the conventional constant-time slices (gray dashed line) to visualize the back-projection volume, which reduces the swimming artifact and alleviates the ambiguity in interpreting subevents.



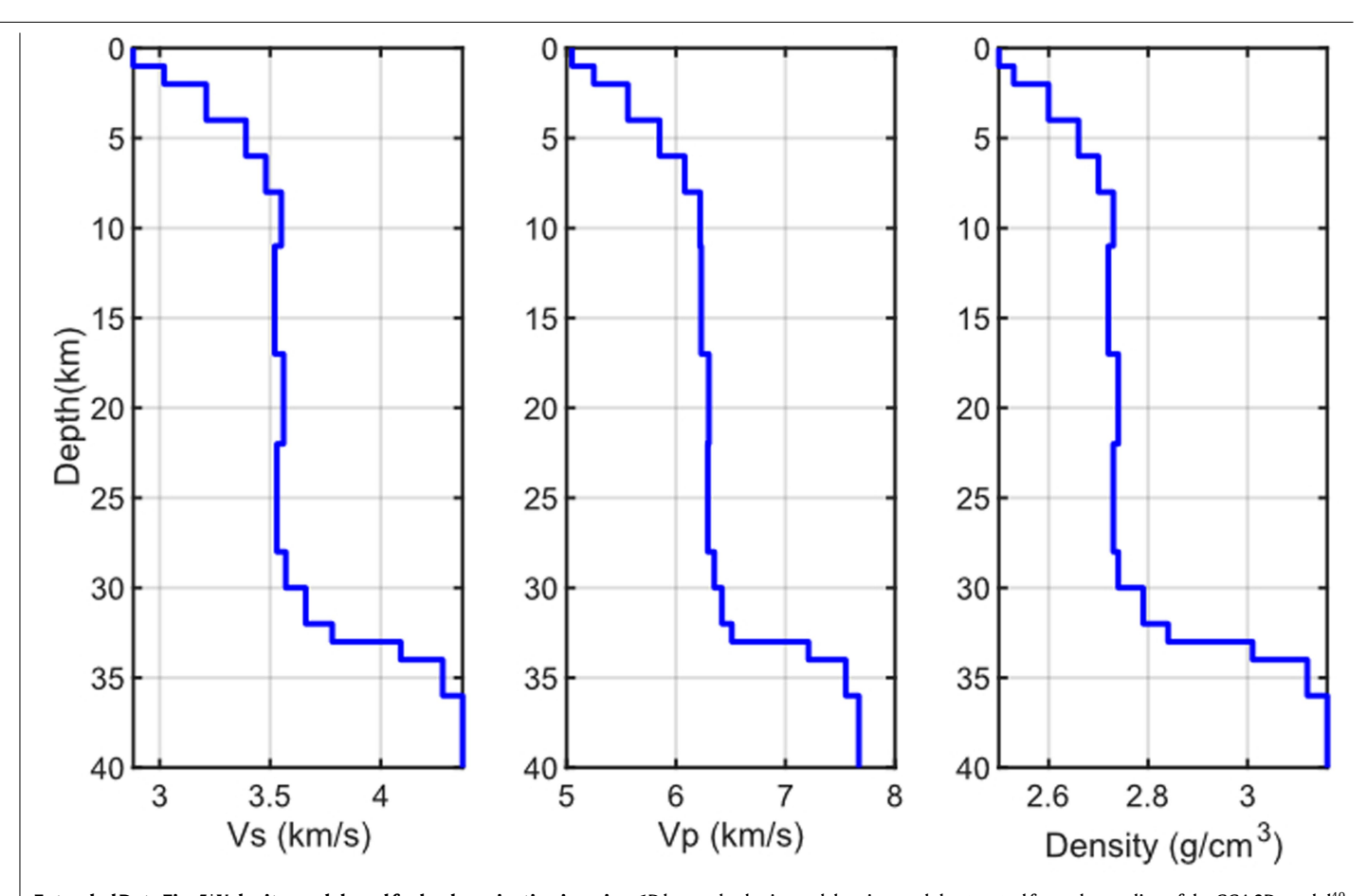
 $\label{lem:extended Data Fig. 3 | Summary of back-projection results. (a-d) \ \text{Map view} of the back-projected correlation value on the finite fault for all four subevents. The contour line represents the slip contour of the USGS finite fault solution. The red dot is the maximum cross-correlation value in the 3D volume. The blue dot is the maximum cross-correlation value on the finite-fault plane. (e-h) Vertical cross-section of the back-projected correlation value for all four subevents. The yellow swath in panels e-h is caused by the spatial geometry of the earthquake and our DAS array. Another DAS array at a different azimuth would improve the resolution. The red solid line represents the USGS finite-fault plane. The red dot is the location of the global cross-correlation$

maximum. The blue dot is the cross-correlation maximum on the finite fault plane. The scattered orange circles are the aftershocks. i, Subevent time, location, magnitude, and average rupture speed between the subevents and SO. The reference (zero) time is 2021-07-08 22:49:48.41 UTC. The locations are determined by picking the maximum cross-correlation value on the intersection between the finite-fault plane and the back-projected cross-correlation isochrone. The mean and error of the magnitude are calculated based on the scaling relationship at five strong-motion stations (Fig. 1; see Methods). The average rupture speed is calculated from the distance over the traveling time between SO and each of the other three subevents.

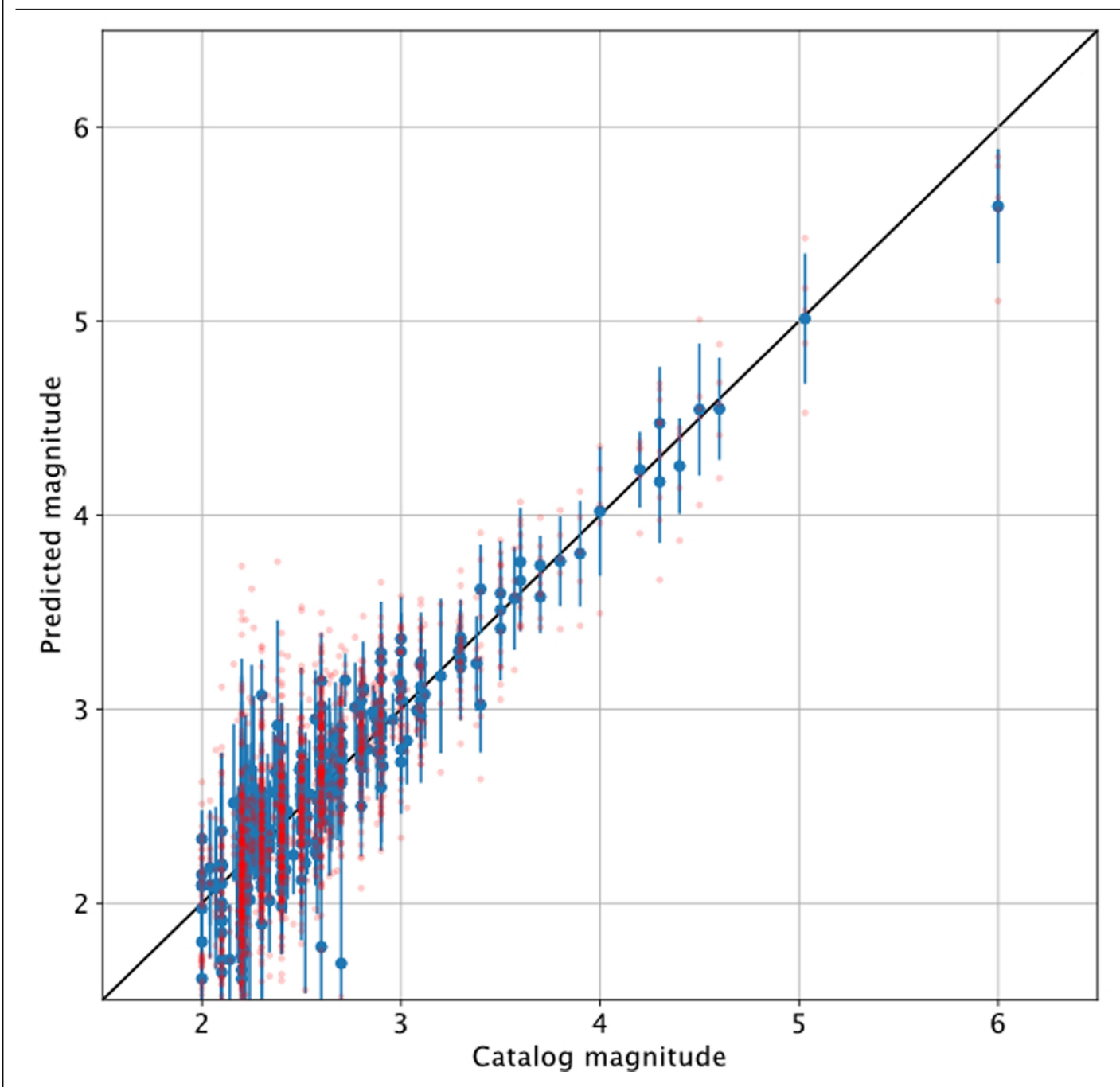


Extended Data Fig. 4 | **Summary of back-projection results continue.** (\mathbf{a} - \mathbf{d}) Correlation time series for P- and S-phases and their average for all four subevents (\mathbf{e} - \mathbf{h}) Three orthogonal slices across the point with the highest correlation in the 3D back-projection volume. The red dot denotes the M6.0 mainshock location, the blue dot denotes the aftershock event used for obtaining the EGF i.e., the M4.2 (event ID NC73585086) aftershock for panels A, E, and the M3.7 (event ID NC73585056) aftershock for panels (\mathbf{b} - \mathbf{d}) and (\mathbf{f} - \mathbf{h}). Since we use

a higher frequency band of 4–8 Hz for subevent 'SO', compared with 1–5Hz for subevents 'S1–3', the cross-correlation time series in (\mathbf{a}) show more wiggles than (\mathbf{b} – \mathbf{d}). Incidentally, the back-projection imaging at higher frequencies could bring higher resolution but may cause lower robustness due to cycle skipping. Later subevents would also be more difficult to image due to stronger attenuation at higher frequencies.

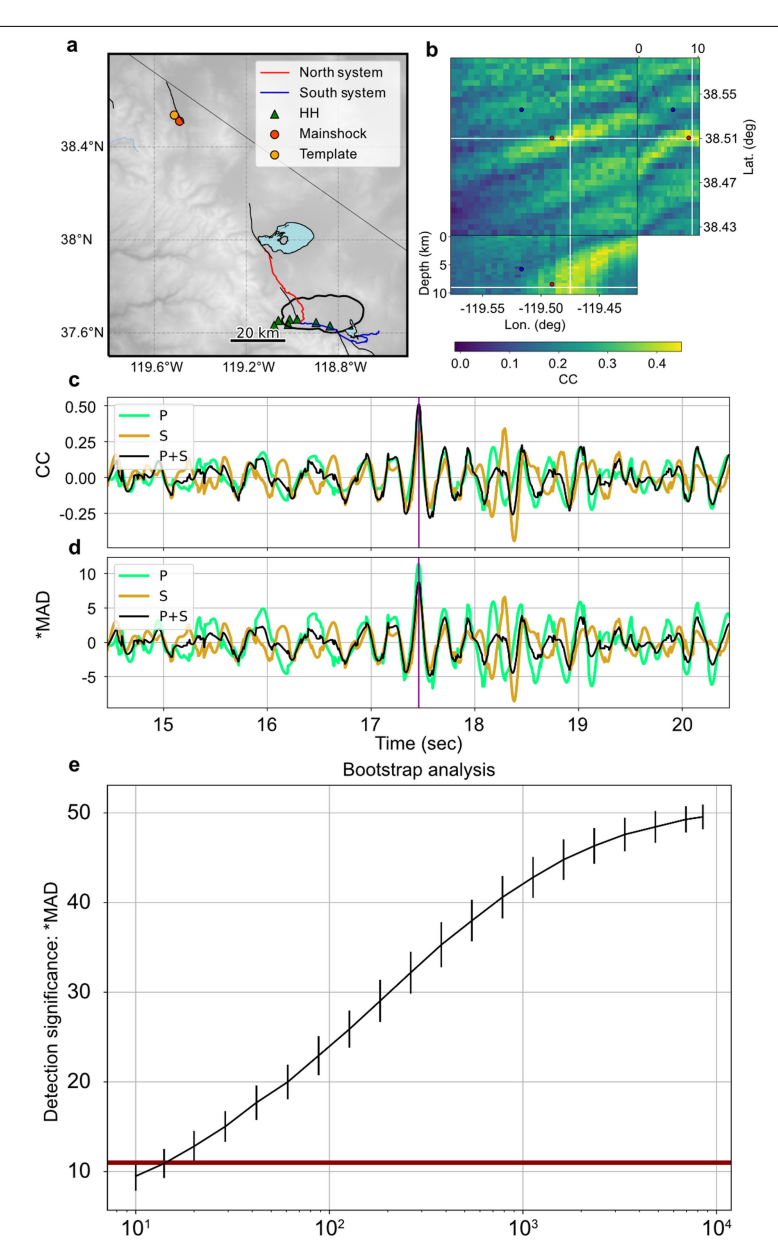


 $\textbf{Extended Data Fig. 5} | \textbf{Velocity model used for back-projection imaging.} 1D \ layered \ velocity \ and \ density \ model \ extracted \ from \ the \ median of the CCA 3D \ model^{40}.$ At the depth of the M6.0 main shock, the shear wave velocity is about 3.5 km/s. We use this 1D velocity model to extract the after shock P and S windows.



 $\label{lem:extended} \textbf{ Data Fig. 6} \ | \ \textbf{ Calculate magnitude through empirical scaling relationship.} \ Comparison between the predicted magnitude with the catalog magnitude based on the scaling relationship described in Methods. The red dots represent the predicted magnitude at each strong-motion station. For each$

earthquake event, the blue dot and vertical bar represent the mean and standard deviation of predicted magnitude at five strong-motion stations. The predicted magnitudes are close to the catalog magnitudes (scatter around the black diagonal line).

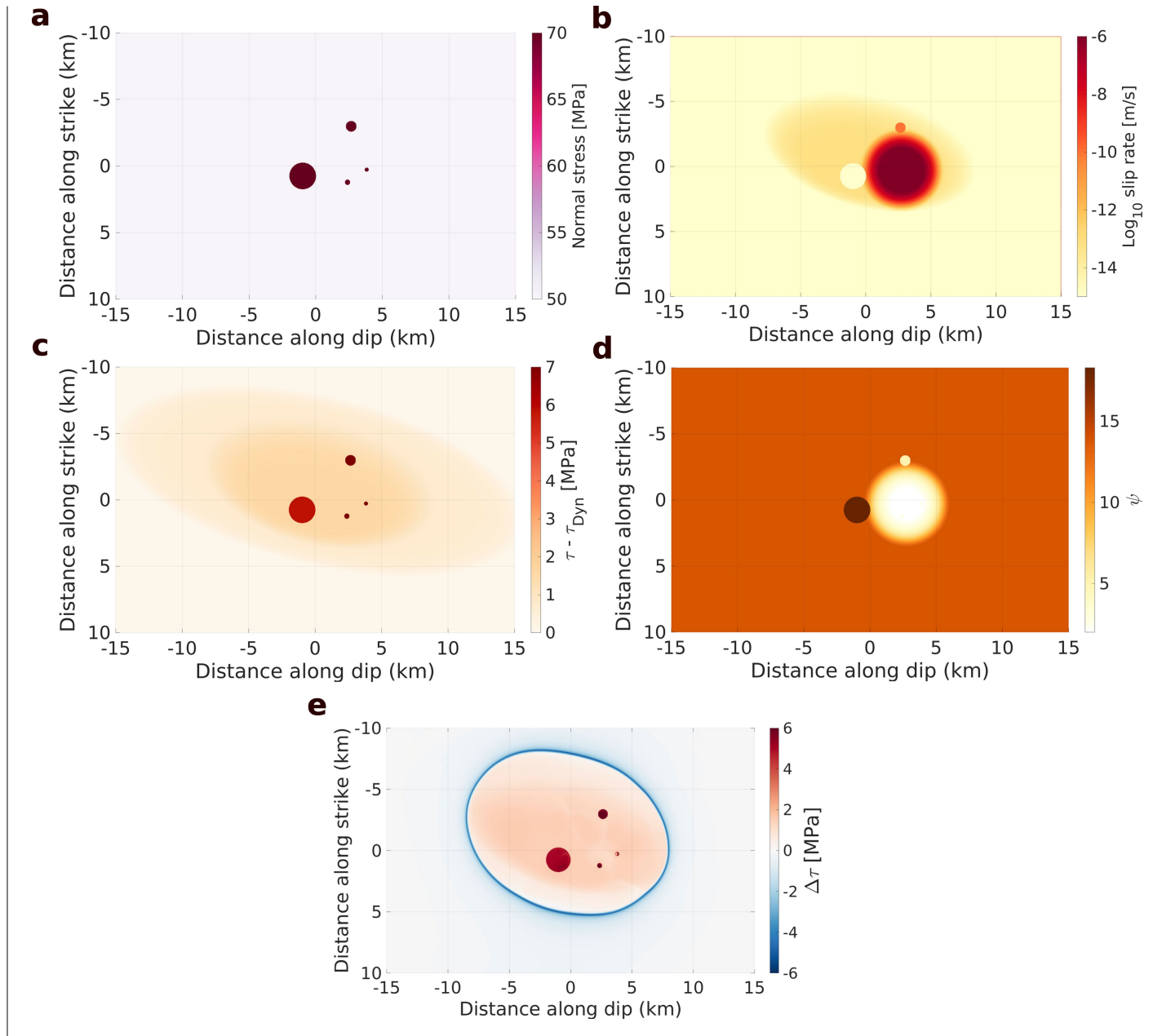


Extended Data Fig. 7 | Back-projection imaging with conventional stations. a, Location of high-broadband stations (green triangles). b, Three orthogonal slices through the point with the highest correlation in the 3D back-projection volume, with the red dot denoting the location of the M6.0 event, and the blue dot denoting the aftershock used for the EGF. c, Cross-correlation time series for the grid point with the highest cross-correlation value. d, *MAD time series

for the grid point with the highest cross-correlation value. **e**, Bootstrap analysis of *MAD increasing with the number of channels used for stacking. The vertical bar represents the standard deviation of the *MAD. The horizontal dark red line represents the detection significance (*MAD = 11) using seven broadband stations following the same imaging procedure. Note that the horizontal axis is on the log scale.

| t=-0.40 sec | t=0.00 sec | t=0.40 sec | t=0.80 sec | t=1.20 sec |
|--------------------|------------|------------|------------|------------|
| 0 0 ° ° 5 km | · · · | ° .• | ° • | \circ |
| t=1.60 sec | t=2.00 sec | t=2.40 sec | t=2.80 sec | t=3.20 sec |
| | | | | |
| t=3.60 sec | t=4.00 sec | t=4.40 sec | t=4.80 sec | t=5.20 sec |
| • | | 0 | 0. | |
| t=5.60 sec | t=6.00 sec | t=6.40 sec | t=6.80 sec | t=7.20 sec |
| t=7.60 sec | t=8.00 sec | t=8.40 sec | t=8.80 sec | t=9.20 sec |
| 0 | 0 | | | 0.: |

Extended Data Fig. 8 | Snapshots of slip-rate distribution for model 1. The rupture initiates around the first asperity. The rupture of each asperity results first in a rupture delay and then in a splash of additional slip with faster rupture speed; the effect is most pronounced for the largest fourth asperity.



Extended Data Fig. 9 | Distribution of initial parameters and final stress drop for the numerical simulation of model 1 with four asperities. a, The normal stress level within the asperities is higher than in the background. b, Distribution of the initial slip rate. c, The distribution of the initial shear

stress over the dynamic level. **d**, Distribution of $\psi = \frac{V^*\theta}{D_{RS}}$. **e**, Final stress drop distribution after rupture arrest. The average stress drop is 1.4 MPa. The stress drop within the asperities ranges from 5.0 to 6.1 MPa.

Extended Data Table 1 | Rupture model parameters

| Parameter | | Sy | Symbol | | Value | |
|------------------------------------|------------|--------------------|-------------------|---------|----------------------|--|
| Shear Wave Speed | | | c_S | | 3700 m/s | |
| Shear Modulus | | | μ | | 38.2 GPa | |
| P Wave Speed | | | c_P | | 6400 m/s | |
| Effective Normal Stress | | | σ | | 50 MPa | |
| | Rate-and-S | State Parameters | of outside of asp | erities | | |
| Reference Slip Velocity | | | V * | | 10 ⁻⁶ m/s | |
| Reference Friction Coefficient | | | f^* | | 0.6 | |
| Rate-and-State Direct Effect | | | а | | 0.003 | |
| Rate-and-State Evolution Effect | | | b | | 0.00455 | |
| Characteristic Slip Distance | | i | D_{RS} | | 1.6 mm | |
| | Lengt | th Scales of the B | ackground Mode | I | | |
| Quasi-Static-Cohesive Zone | | | Λ_0 | | 237 m | |
| Nucleation Size | | | h^* | 3636 m | | |
| Cell Size | | Δ_z | | 25 m | | |
| Property | S0 | S1 | S1 S2 | | S3 | |
| | | | | Model 1 | Model 3 | |
| σ (MPa) | | | 70 | | | |
| Radius (km) | 0.15 | 0.2 | 0.4 | 1.0 | | |
| a | 0.003 | 0.003 | 0.003 | 0.0049 | 0.003 | |
| b | | | 0.010 | | | |
| $V_{ini} (\log_{10} \mathrm{m/s})$ | -5.9 | -5.9 | -10 | -20 | | |
| h * (m) | 280 | 280 | 280 | 527 | 280 | |
| Λ_0 (m) | | | 77 | | | |

 $[\]pmb{a}\text{, Properties of the bulk and the fault around the asperities.}\, \pmb{b}\text{, Properties of the asperities.}$